Multi-scale indentation model of stiff film-compliant substrate structures

Yanwei Liu [a], Hansong Ma [b], Hao Long [a], Shiyuan Wei [c,d], Siyuan Zhang [e], Yueguang Wei [a,*]

[a] Department of Mechanics and Engineering Science, College of Engineering, BIC-ESAT, Peking University, Beijing 100871, PR China
[b] State-Key Laboratory of Nonlinear Mechanics, Institute of Mechanics, Chinese Academy of Sciences, Beijing 100190, PR China
[c] Department of Biomedical Engineering, College of Engineering, Peking University, Beijing 100871, PR China
[d] China Academy for Advanced Interdisciplinary Studies, Peking University, Beijing 100871, PR China
[e] School of Mechanical Engineering, University of Shanghai for Science and Technology, Shanghai 200093, PR China

ARTICLE INFO

ABSTRACT

As critical components or platforms, stiff film-compliant substrate structures are widely used in micro-electro-mechanical systems (MEMS) and other devices, in which their indentation behavior plays an important role. In this work, a multi-scale indentation model (MSI) for stiff film-compliant substrate structures is established based on the strain gradient theory and the surface elastic model. With this model, the indentation size effect of the structure is investigated from three aspects: the load-depth relationship, the distribution of bending moments in the film, and the surface morphology. The results show that the indentation size effect is mainly caused by the characteristic length and the surface residual stress of the film, and it is sensitive to the modulus ratio of the film to the substrate but has little relation with Poisson's ratio and the contact radius. Based on the above analysis, two dimensionless numbers are proposed to evaluate the indentation size effect of stiff film-compliant substrate structures. Besides, the predicted bending stiffness by the theoretical model is consistent with the experimental result, which verifies the effectiveness of the MSI model. Our research sheds light on the understanding of the indentation size effect of stiff film-compliant substrate structures and provides theoretical guidance for the design of related devices.

1. Introduction

Due to their extensive applications in MEMS [1–5] and scientific research [6–9], the stiff film-compliant substrate structures have ignited the enthusiasm of researchers. In these applications, the mechanical behavior of stiff film-compliant substrate structures, especially the indentation behavior, plays an essential role [10–13]. For example, Ho et al. [1] fabricated a stretchable electronic skin by laying graphene oxide (GO) and its reduced form (rGO) on polydimethylsiloxane (PDMS), and the electronic skin can sensor different out-of-plane pressures by different electrical signals; to avoid the non-linear effects, Liu et al. [8] proposed a novel method to measure the mechanical properties of soft matters by the indentation response of stiff film-compliant substrate structures; Niu et al. [7] characterized the fracture properties of graphene through the in-

---

* Corresponding author.
  E-mail address: weiyg@pku.edu.cn (Y. Wei).

dentation response of graphene-PDMS structures. Therefore, an in-depth understanding of the indentation behavior of stiff film-compliant substrate structures will contribute to their comprehensive applications.

To promote their applications, it is necessary to establish theoretical models to quantitatively describe the indentation behavior of this structure. At the macro scale, various models have been established by researchers. For example, based on the analysis of a large number of indentation data, an empirical model with a weighted average was proposed by Doerner and Nix [14]. Because there are empirical parameters related to the geometry of the indenter in the model, it is not convenient for practical applications. After that, Gao et al. [15] developed an approximate model based on the perturbation analysis, and this model was modified by Xu and Pharr [16] to improve its range of applicability. This approximate model was in good agreement with the simulation result only when $1/3 < E_f/E_s < 3$ (E_f and E_s are the moduli of the film and the substrate, respectively). Considering this case, Gao et al. [17] derived an analytical indentation model with the exact solution of Green's function in the Fourier space, and this analytical model is suitable for the case where $0.1 < E_f/E_s < 10$. For the stiff film-compliant substrate structures with $E_f/E_s > 10^2$, both Liu et al. [18] and Box et al. [19] obtained the analytical indentation solution by the Hankel transform, but the former avoided solving the pair of integral equations by assuming a uniform stress distribution under the indenter.

With the development of science and technology, the size of stiff film-compliant substrate structures widely used in MEMS and scientific research becomes smaller and smaller than before [20–22]. For example, the thickness of GO or rGO placed on PDMS to fabricate the electronic skin is into the nanometer scale [1]; the thickness of the film mounted on a compliant substrate to form a test platform to measure the mechanical properties of soft matter is also into the nanometer scale [8]. Therefore, the indentation response of stiff film-compliant substrate structures at the micro/nano scale has received extensive attention in recent years. At the micro scale, the high-order continuum theory is considered to be an effective method to describe the size effect of mechanical behaviors of materials because of its ability to capture the microstructure effects [23–29]. With this idea, the strain gradient theory has been widely used to investigate the indentation size effect of stiff film-compliant substrate structures at the micro scale [30–32]. For example, with the mechanism-based strain gradient theory, Zhang et al. [30] studied the indentation response of stiff film-compliant substrate structures, and they found that the gradient effect in the stiff film is significant but that in the compliant substrate can be neglected, and the strain gradient effect in the stiff film disappeared rapidly with the increase of the indentation depth. In addition, the effects of the substrate and the grain size on the indentation behavior of film-substrate structures were analyzed by Chen et al. [31]. In the above studies, E_f/E_s is lower than 10, and there are few studies on the indentation size effect of stiff film-compliant substrate structures with $E_f/E_s > 10^2$. Considering this case, Liu et al. [32] derived an analytical indentation model for stiff film-compliant substrate structures with $E_f/E_s > 10^2$ based on the strain gradient theory and investigated the effect of the characteristic length on the indentation response. Apart from the influence of the strain gradient, many studies have shown that surface energy also has significant effects on the mechanical behavior of materials at the micro scale [23,33–38]. As far as we know, for the stiff film-compliant substrate structures with $E_f/E_s > 10^2$, the coupling effect of the strain gradient and the surface energy on the indentation response has not been investigated in detail. It is also unclear that how these effects influence the indentation behavior when the structure size changes from macro scale to micro/nano scale.

To understand the indentation size effect of stiff film-compliant substrate structures with a high modulus ratio and to quantitatively describe it, in this work, a MSI model is established based on the strain gradient theory and the surface elastic model. With the model, the multi-scale indentation response of stiff film-compliant substrate structures is investigated. It needs to be emphasized that compared with our previous work [32], we further consider the effect of surface energy in the present work, and the coupling effect of the strain gradient and the surface energy is investigated. The arrangement of this paper is as follows: In Section 2, the derivation process of the MSI model is introduced. In Section 3, based on the model, the effects of the strain gradient and the surface energy on the indentation response of stiff film-compliant substrate structures are analyzed, and the dominant factors causing the indentation size effect are obtained at different scales. In Section 4, the influences of E_f/E_s, contact radius, and Poisson's ratio on the indentation size effect are discussed. Based on the above analysis, two dimensionless numbers are proposed to describe the effects of the strain gradient and the surface energy. In Section 5, the bending stiffness of the film predicted by the MSI model is compared with the experiment result to validate the effectiveness of the model. Finally, the main conclusions are summarized in Section 6. Our research sheds light on the understanding of the indentation size effect of stiff film-compliant substrate structures and contributes to comprehensive applications of this structure.

2. Theory and model

The sketch of the stiff film-compliant substrate structure is shown in Fig. 1. Here, the radius of the film and the thickness of the substrate is far greater than the film thickness. For the indentation response of this structure, the previous study has shown that the gradient effect in the stiff film is significant but that in the soft substrate can be neglected [30]. Therefore, we considered the stiff film as a strain gradient elastic material and the compliant substrate as a traditional elastic material. In addition, when E_f/E_s is high ($E_f/E_s > 10^2$), the sink-down phenomenon is obvious when the indenter is pressed into the structure. At this time, the deformation mode of the film is similar to the bending of a plate when the indentation depth is smaller than the film thickness [18,19,39]. Therefore, with the consideration of the surface effect, the indentation response of the stiff film-compliant substrate structure can be regarded as the bending of a strain gradient plate with surface energy mounted on a compliant infinite substrate. In this section, the derivation process of the MSI model is introduced. Firstly,
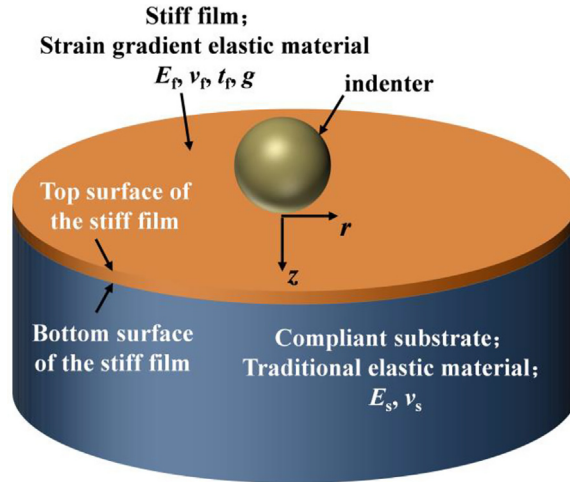
Fig. 1. The sketch of the stiff film-compliant substrate structure.

the governing equation is obtained based on the variational principle. Then, with the Hankel transform, the relationship between load and film deflection is derived. Finally, the bending moment distribution in the film is calculated.

2.1. The governing equation for the indentation response of the stiff film-compliant substrate structure

In this work, we assume that the film is a strain gradient Kirchhoff plate with surface energy. Based on Kirchhoff's hypothesis, the film deflection is only a function of x and y. Then, the strains in the plate read

$$\varepsilon_{xx} = -z\frac{\partial^2 w}{\partial x^2}, \varepsilon_{yy} = -z\frac{\partial^2 w}{\partial y^2}, \varepsilon_{xy} = -z\frac{\partial^2 w}{\partial x\partial y} \tag{1}$$

where w is the film deflection. Based on the simplified theory of strain gradient linear elasticity [40,41] due to Mindlin [42], the constitutive equations are

$$\begin{aligned} \boldsymbol{\sigma} &= 2\mu\boldsymbol{\varepsilon} + \lambda\mathrm{tr}\boldsymbol{\varepsilon}\boldsymbol{I} \\ \boldsymbol{\tau} &= \mathrm{g}^2\nabla\boldsymbol{\sigma} \\ \boldsymbol{\Sigma} &= \boldsymbol{\sigma} - \nabla\cdot\boldsymbol{\tau} \end{aligned} \tag{2}$$

where $\boldsymbol{\sigma}$ is the classical Cauchy stress tensor, $\boldsymbol{\tau}$ is the double stress tensor, $\boldsymbol{\Sigma}$ is the total stress tensor, $\boldsymbol{\varepsilon} = 1/2(\nabla u + u\nabla)$ is the strain tensor, $\mathrm{tr}\boldsymbol{\varepsilon}$ is its trace, λ and μ are Lame constants, $\boldsymbol{I}$ is a unit tensor, and g is the characteristic length of material. Based on Kirchhoff's hypothesis, only in-plane stresses are considered. According to Eq. (2), the Cauchy stress and the double stress in the plane can be written as

$$\sigma_{xx} = \frac{E_f}{1-v_f^2}(\varepsilon_{xx}+v\varepsilon_{yy}), \tau_{xxx} = g^2\frac{E_f}{1-v_f^2}\frac{\partial(\varepsilon_{xx}+v\varepsilon_{yy})}{\partial x}, \tau_{xxy} = g^2\frac{E_f}{1-v_f^2}\frac{\partial(\varepsilon_{xx}+v\varepsilon_{yy})}{\partial y} \tag{3a}$$

$$\sigma_{yy} = \frac{E_f}{1-v_f^2}(\varepsilon_{yy}+v\varepsilon_{xx}), \tau_{yyx} = g^2\frac{E_f}{1-v_f^2}\frac{\partial(\varepsilon_{yy}+v\varepsilon_{xx})}{\partial x}, \tau_{yyy} = g^2\frac{E_f}{1-v_f^2}\frac{\partial(\varepsilon_{yy}+v\varepsilon_{xx})}{\partial y} \tag{3b}$$

$$\sigma_{xy} = \frac{E_f}{1+v_f}\varepsilon_{xy}, \tau_{xyx} = g^2\frac{E_f}{1+v_f}\frac{\partial\varepsilon_{xy}}{\partial x}, \tau_{xyy} = g^2\frac{E_f}{1+v_f}\frac{\partial\varepsilon_{xy}}{\partial y} \tag{3c}$$

where E_f and v_f are the elastic modulus and Poisson's ratio of the stiff film, respectively. Then, the strain energy in the stiff film reads

$$\begin{aligned} U_1 &= \frac{1}{2}\iiint \sigma_{xx}\varepsilon_{xx} + \sigma_{yy}\varepsilon_{yy} + 2\sigma_{xy}\varepsilon_{xy}dxdydz \\ &+ \frac{1}{2}\iiint \tau_{xxx}\varepsilon_{xx,x} + 2\tau_{xyx}\varepsilon_{xy,x} + \tau_{yyx}\varepsilon_{yy,x} + \tau_{xxy}\varepsilon_{xx,y} + 2\tau_{xyy}\varepsilon_{xy,y} + \tau_{yyy}\varepsilon_{yy,y}dxdydz \end{aligned} \tag{4}$$

Using Eqs. (1) and (3) in (4), and performing variational calculations on Eq. (4), one can get

$$\begin{aligned} \delta U_1 &= \iint_A (D\nabla^4 w - g^2 D\nabla^6 w)\delta w dxdy \\ &+ \int_S (D\Xi_1 + g^2 D\Xi_2)\frac{\partial\delta w}{\partial n}ds + \int_S g^2 D\Xi_3\frac{\partial^2\delta w}{\partial n^2}ds + \int_S (D\Theta_1 + g^2 D\Theta_2)\delta w ds \end{aligned} \tag{5}$$

where $D = (E_f t_f^3)/[12(1-v_f^2)]$ is the bending stiffness of the film, and t_f is the film thickness. The detailed derivation of Eq. (5) can be found in Appendix A. Ξ_1, Ξ_2, Ξ_3, Θ_1, and Θ_2 are

$$\Xi_1 = (\frac{\partial^2 w}{\partial x^2} + v_f\frac{\partial^2 w}{\partial y^2})\cos^2\alpha + (\frac{\partial^2 w}{\partial y^2} + v_f\frac{\partial^2 w}{\partial x^2})\sin^2\alpha + 2(1-v_f)\frac{\partial^2 w}{\partial x\partial y}\cos\alpha\sin\alpha \tag{6a}$$

$$
\begin{aligned}
\Xi_2 = {}& 2\frac{\partial}{\partial s}\left(\frac{\partial^3 w}{\partial x^3}\sin\alpha\cos^2\alpha\right) - \frac{\partial^4 w}{\partial x^4}\cos^2\alpha - 2\frac{\partial}{\partial s}\left(\frac{\partial^3 w}{\partial y^3}\cos\alpha\sin^2\alpha\right) - \frac{\partial^4 w}{\partial y^4}\cos^2\alpha \\
& - 3\frac{\partial^4 w}{\partial x^2\partial y^2}\sin^2\alpha - 6\frac{\partial}{\partial s}\left(\frac{\partial^3 w}{\partial x\partial y^2}\sin\alpha\cos^2\alpha\right) - 3\frac{\partial^4 w}{\partial x^2\partial y^2}\cos^2\alpha \\
& + 6\frac{\partial}{\partial s}\left(\frac{\partial^3 w}{\partial x^2\partial y}\cos\alpha\sin^2\alpha\right) - v_f\frac{\partial}{\partial s}\left[(\cos^2\alpha - \sin^2\alpha)(\cos\alpha(\frac{\partial^3 w}{\partial y^3} - \frac{\partial^3 w}{\partial x^2\partial y})\right. \\
& \left. - \sin\alpha(\frac{\partial^3 w}{\partial x\partial y^2} - \frac{\partial^3 w}{\partial x^3})) + 4\sin\alpha\cos\alpha(\frac{\partial^3 w}{\partial x^2\partial y}\sin\alpha - \frac{\partial^3 w}{\partial x\partial y^2}\cos\alpha)\right]
\end{aligned}
\tag{6b}
$$

$$
\begin{aligned}
\Xi_3 = {}& \frac{\partial^3 w}{\partial x^3}\cos^3\alpha + \frac{\partial^3 w}{\partial y^3}\sin^3\alpha + 3\frac{\partial^3 w}{\partial x\partial y^2}\sin^2\alpha\cos\alpha \\
& + 3\frac{\partial^3 w}{\partial x^2\partial y}\cos^2\alpha\sin\alpha + v_f(\cos^2\alpha - \sin^2\alpha)(\frac{\partial^3 w}{\partial x\partial y^2}\cos\alpha - \frac{\partial^3 w}{\partial x^2\partial y}\sin\alpha) \\
& + v_f\cos\alpha\sin\alpha(\cos\alpha(\frac{\partial^3 w}{\partial y^3} - \frac{\partial^3 w}{\partial x^2\partial y}) - \sin\alpha(\frac{\partial^3 w}{\partial x\partial y^2} - \frac{\partial^3 w}{\partial x^3}))
\end{aligned}
\tag{6c}
$$

$$
\begin{aligned}
\Theta_1 = {}& -\left(\frac{\partial^3 w}{\partial x^3} + \frac{\partial^3 w}{\partial x\partial y^2}\right)\cos\alpha - \left(\frac{\partial^3 w}{\partial y^3} + \frac{\partial^3 w}{\partial x\partial y^2}\right)\sin\alpha \\
& + (1 - v_f)\frac{\partial}{\partial s}\left((\frac{\partial^2 w}{\partial x^2} - \frac{\partial^2 w}{\partial y^2})\sin\alpha\cos\alpha + \frac{\partial^2 w}{\partial x\partial y}(\sin^2\alpha - \cos^2\alpha)\right)
\end{aligned}
\tag{6d}
$$

$$
\begin{aligned}
\Theta_2 = {}& \frac{\partial^2}{\partial s^2}\left(\frac{\partial^3 w}{\partial x^3}\cos\alpha\sin^2\alpha\right) - \frac{\partial}{\partial s}\left(\frac{\partial^4 w}{\partial x^4}\cos\alpha\sin\alpha\right) + \frac{\partial^5 w}{\partial x^5}\cos\alpha + \frac{\partial^2}{\partial s^2}\left(\frac{\partial^3 w}{\partial y^3}\cos^2\alpha\sin\alpha\right) \\
& + \frac{\partial}{\partial s}\left(\frac{\partial^4 w}{\partial y^4}\cos\alpha\sin\alpha\right) + \frac{\partial^5 w}{\partial y^5}\sin\alpha + 3\frac{\partial^2}{\partial s^2}\left(\frac{\partial^3 w}{\partial x\partial y^2}\cos^3\alpha\right) + 3\frac{\partial}{\partial s}\left(\frac{\partial^4 w}{\partial x^2\partial y^2}\cos\alpha\sin\alpha\right) \\
& + 3\frac{\partial^5 w}{\partial x^2\partial y^3}\sin\alpha + 3\frac{\partial^2}{\partial s^2}\left(\frac{\partial^3 w}{\partial x^2\partial y}\sin^3\alpha\right) + 3\frac{\partial^5 w}{\partial y^2\partial x^3}\cos\alpha - 3\frac{\partial}{\partial s}\left(\frac{\partial^4 w}{\partial x^2\partial y^2}\cos\alpha\sin\alpha\right) \\
& - \frac{\partial^2}{\partial s^2}\left[(\cos^2\alpha - \sin^2\alpha)(\frac{\partial^3 w}{\partial x\partial y^2}\cos\alpha - \frac{\partial^3 w}{\partial x^2\partial y}\sin\alpha) + \sin\alpha\cos\alpha(\cos\alpha(\frac{\partial^3 w}{\partial y^3} - \frac{\partial^3 w}{\partial y\partial x^2})\right. \\
& \left. - \sin\alpha(\frac{\partial^3 w}{\partial x\partial y^2} - \frac{\partial^3 w}{\partial x^3}))\right]
\end{aligned}
\tag{6e}
$$

We assumed that the top surface and the bottom surface of the film have the same mechanical properties, which is reasonable and accepted by previous researchers [43]. The constitutive equation for the surface [44] is

$$
\tau_{\alpha\beta} = \tau_0\delta_{\alpha\beta} + (\tau_0 + \lambda^s)u^s_{\gamma,\gamma}\delta_{\alpha\beta} + (\mu^s - \tau_0)(u^s_{\alpha,\beta} + u^s_{\beta,\alpha}) + \tau_0 u^s_{\alpha,\beta}
\tag{7}
$$

where τ_0 is the residual surface stress, $\tau_{\alpha\beta}$ is the surface stress tensor, λ^s and μ^s are the surface elastic constants, and u^s is the displacement of the film surface. Then, the strain energy of the film surface reads

$$
U_2 = \frac{1}{2}\left(\int_{S^+}\tau_{xx}\varepsilon^{s+}_{xx} + \tau_{yy}\varepsilon^{s+}_{yy} + 2\tau_{xy}\varepsilon^{s+}_{xy}dS^+ + \int_{S^-}\tau_{xx}\varepsilon^{s-}_{xx} + \tau_{yy}\varepsilon^{s-}_{yy} + 2\tau_{xy}\varepsilon^{s-}_{xy}dS^-\right)
\tag{8}
$$

where ε^{s+}_{xx}, ε^{s+}_{yy}, and ε^{s+}_{yx} are the strains of the top surface of the film; ε^{s-}_{xx}, ε^{s-}_{yy}, and ε^{s-}_{yx} are the strains of the bottom surface of the film. Based on Eq. (1), they can be written as

$$
\varepsilon^{s+}_{xx} = \frac{t_f}{2}\frac{\partial^2 w}{\partial x^2}, \varepsilon^{s+}_{yy} = \frac{t_f}{2}\frac{\partial^2 w}{\partial y^2}, \varepsilon^{s+}_{xy} = \frac{t_f}{2}\frac{\partial^2 w}{\partial x\partial y}
\tag{9a}
$$

$$
\varepsilon^{s-}_{xx} = -\frac{t_f}{2}\frac{\partial^2 w}{\partial x^2}, \varepsilon^{s-}_{yy} = -\frac{t_f}{2}\frac{\partial^2 w}{\partial y^2}, \varepsilon^{s-}_{xy} = -\frac{t_f}{2}\frac{\partial^2 w}{\partial x\partial y}
\tag{9b}
$$

Substituting Eqs. (7) and (9) into (8), we can get

$$
U_2 = \iint \frac{(\lambda^s + 2\mu^s)t_f^2}{4}(\nabla^2 w)^2 - \frac{t^2(2\mu^s - \tau_0^s)}{2}(w_{,xx}w_{,yy} - w_{,xy}^2)dxdy
\tag{10}
$$

The variation of the elastic strain energy of the film surface is as follows (See Appendix B for the detailed derivation):

$$
\delta U_2 = \iint \frac{(\lambda^s + 2\mu^s)t_f^2}{2}\nabla^4 w\delta w dxdy + \int_S \Psi_1\delta w ds + \int_S \Psi_2\frac{\partial\delta w}{\partial n}ds
\tag{11}
$$

where

$$
\begin{aligned}
\Psi_1 = {}& \frac{(\lambda^s + 2\mu^s)t_f^2}{2}\left\{\begin{array}{l}[\frac{\partial}{\partial s}(\frac{\partial^2 w}{\partial x^2}\sin\alpha\cos\alpha) - \frac{\partial^3 w}{\partial x^3}\cos\alpha] - \{\frac{\partial^3 w}{\partial x^2\partial y}\sin\alpha \\ + \frac{\partial^3 w}{\partial x\partial y^2}\cos\alpha + \frac{\partial}{\partial s}[(\frac{\partial^2 w}{\partial x^2} - \frac{\partial^2 w}{\partial y^2})\sin\alpha\cos\alpha]\} \\ -[\frac{\partial}{\partial s}(\frac{\partial^2 w}{\partial y^2}\sin\alpha\cos\alpha) + \frac{\partial^3 w}{\partial y^3}\sin\alpha]\end{array}\right\} \\
& + \frac{t_f^2(2\mu^s - \tau_0^s)}{2}\left\{\begin{array}{l}\{\frac{\partial^3 w}{\partial x^2\partial y}\sin\alpha + \frac{\partial^3 w}{\partial x\partial y^2}\cos\alpha + \frac{\partial}{\partial s}[(\frac{\partial^2 w}{\partial x^2} - \frac{\partial^2 w}{\partial y^2}) \\ \sin\alpha\cos\alpha]\} + \{\frac{\partial}{\partial s}[\frac{\partial^2 w}{\partial x\partial y}(\sin^2\alpha - \cos^2\alpha)] \\ - \frac{\partial^3 w}{\partial x\partial y^2}\cos\alpha - \frac{\partial^3 w}{\partial x^2\partial y}\sin\alpha\}\end{array}\right\}
\end{aligned}
\tag{12a}
$$

$$
\begin{aligned}
\Psi_2 = {}& \frac{(\lambda^s + 2\mu^s)t_f^2}{2}[\frac{\partial^2 w}{\partial x^2}\cos^2\alpha + (\frac{\partial^2 w}{\partial y^2}\cos^2\alpha + \frac{\partial^2 w}{\partial x^2}\sin^2\alpha) + \frac{\partial^2 w}{\partial y^2}\sin^2\alpha] \\
& - \frac{t_f^2(2\mu^s - \tau_0^s)}{2}[(\frac{\partial^2 w}{\partial y^2}\cos^2\alpha + \frac{\partial^2 w}{\partial x^2}\sin^2\alpha) - 2\frac{\partial^2 w}{\partial x\partial y}\sin\alpha\cos\alpha]
\end{aligned}
\tag{12b}
$$

Based on Eqs. (5) and (11), we can know that the variation of the total elastic strain energy of the film is

$$
\begin{aligned}
\delta U = \delta U_1 + \delta U_2 = &\iint_A [(D + \tfrac{(\lambda^s + 2\mu^s)t_f^2}{2})\nabla^4 w - g^2 D \nabla^6 w]\delta w dx dy \\
&+ \int_S (D\Xi_1 + g^2 D\Xi_2 + \Psi_1)\tfrac{\partial \delta w}{\partial n}ds + \int_S g^2 D\Xi_3 \tfrac{\partial^2 \delta w}{\partial n^2}ds \\
&+ \int_S (D\Theta_1 + g^2 D\Theta_2 + \Psi_2)\delta w ds
\end{aligned}
\tag{13}
$$

Eq. (13) suggests the work δW done by the external force is

$$
\delta W = \iint_A (q + q^s - p)\delta w dx dy - \int_S M_n \frac{\partial \delta w}{\partial n}ds - \int_S M_{nn}\frac{\partial^2 \delta w}{\partial n^2}ds + \int_S V_n \delta w ds
\tag{14}
$$

where q is the indentation load, p is the reaction force of the substrate to the film, M_n is the traditional moment, M_{nn} is the high-order moment, V_n is the concentration force acting on the film, and $q^s = 2\tau_0 \nabla^2 w$ is the force due to the change of the surface curvature. The reason why we introduce q^s into Eq. (14) is as follows: when the surface effect is considered, the discontinuity of the stress across the interface follows the generalized Yang-Laplace equation [45–48]:

$$
\Delta \sigma_{ij} n_i n_j = \tau_{\alpha\beta}^s \kappa_{\alpha\beta}^s
\tag{15}
$$

where $\Delta \sigma_{ij} = \sigma_{ij}^2 - \sigma_{ij}^1$ denotes the discontinuity of the stress across the interface, $\tau_{\alpha\beta}^s$ is the surface stress, $\kappa_{\alpha\beta}^s$ is the curvature tensor of the surface, and n_i is the normal vector of the film surface. With Eq. (15), the additional force can be expressed as $q^s = 2\tau_0 \nabla^2 w$. Including the residual stress in the mechanical description by this method has been proven to be effective by experiments [46,49–51].

For the bending of the strain gradient plate with surface energy mounted on a compliant infinite substrate, according to the energy conversation law $\delta U = \delta W$, the governing equation and boundary conditions can be expressed as

$$
D'\nabla^4 w(x, y) - 2\tau_0 \nabla^2 w(x, y) - g^2 D \nabla^6 w(x, y) = q(x, y) - p(x, y)
\tag{16a}
$$

$$
M_n = D\Xi_1 + g^2 D\Xi_2 + \Psi_1
\tag{16b}
$$

$$
M_{nn} = g^2 D\Xi_3
\tag{16c}
$$

$$
V_n = D\Theta_1 + g^2 D\Theta_2 + \Psi_2
\tag{16d}
$$

where D', $\nabla^2 w(x,y)$, $\nabla^4 w(x,y)$ and $\nabla^6 w(x,y)$ are

$$
D' = D + \frac{(\lambda^s + 2\mu^s)t_f^2}{2}
\tag{17a}
$$

$$
\nabla^2 w(x, y) = \frac{\partial^2 w}{\partial x^2} + \frac{\partial^2 w}{\partial y^2}
\tag{17b}
$$

$$
\nabla^4 w(x, y) = \frac{\partial^4 w}{\partial x^4} + 2\frac{\partial^4 w}{\partial x^2 \partial y^2} + \frac{\partial^4 w}{\partial y^4}
\tag{17c}
$$

$$
\nabla^6 w(x, y) = \frac{\partial^6 w}{\partial x^6} + 3\frac{\partial^6 w}{\partial x^4 \partial y^2} + 3\frac{\partial^6 w}{\partial x^2 \partial y^4} + \frac{\partial^6 w}{\partial y^6}
\tag{17d}
$$

In the case of symmetry, Eq. (16a) can be written as

$$
D'\nabla^4 w(r) - 2\tau_0 \nabla^2 w(r) - g^2 D \nabla^6 w(r) = q(r) - p(r)
\tag{18a}
$$

For the indentation response of the strain gradient plate with surface energy mounted on a compliant substrate, the boundary conditions are

$$
\begin{aligned}
&w(+\infty) = 0, w'(+\infty) = 0, w''(+\infty) = 0 \\
&w(0) = w_0, w'(0) = 0, V_n(0) \neq \infty
\end{aligned}
\tag{18b}
$$

$\nabla^2 w(r)$, $\nabla^4 w(r)$ and $\nabla^6 w(r)$ are given by

$$
\nabla^2 w(r) = \frac{d^2 w}{dr^2} + \frac{1}{r}\frac{dw}{dr}
\tag{19a}
$$

$$
\nabla^4 w(r) = \frac{d^4 w}{dr^4} + \frac{2}{r}\frac{d^3 w}{dr^3} - \frac{1}{r^2}\frac{d^2 w}{dr^2} + \frac{1}{r^3}\frac{dw}{dr}
\tag{19b}
$$

$$
\nabla^6 w(r) = \frac{1}{r}\frac{d}{dr}(r\frac{d}{dr}\nabla^4 w)
\tag{19c}
$$

2.2. The relationship between the indentation load and the film deflection

Based on the Hankel transform, the relationship between the indentation load and the film deflection can be obtained. The detailed process is introduced as follows. The Hankel transform of Eq. (18a) is

$$D'\xi^4\overline{w}(\xi) + 2\tau_0\xi^2\overline{w}(\xi) + g^2D\xi^6\overline{w}(\xi) = \overline{q}(\xi) - \overline{p}(\xi) \tag{20}$$

Moreover, the surface vertical displacement of a semi-infinite solid under an arbitrary symmetric load reads [52]

$$w(r) = \frac{2(1-v_s^2)}{E_s}\int_0^{+\infty}\overline{p}(\xi)J_0(\xi r)d\xi \tag{21}$$

where E_s and v_s are the modulus and Poisson's ratio of the soft substrate, respectively. Here, we assume that the film deflection is coordinated with the surface vertical displacement of the substrate, and there is no slip in the interface. These assumptions are always considered to be reasonable when the indentation depth is no more than the film thickness. Then, combining Eqs. (20) and (21), we can get the film deflection:

$$w(r) = \frac{2(1-v_s^2)}{E_s}\int_0^{+\infty}[\overline{q}(\xi) - D'\xi^4\overline{w}(\xi) - 2\tau_0\xi^2\overline{w}(\xi) - g^2D\xi^6\overline{w}(\xi)]J_0(\xi r)d\xi \tag{22}$$

In addition, the inverse Hankel transform of the film deflection is

$$w(r) = \int_0^{+\infty}\overline{w}(\xi)J_0(\xi r)\xi d\xi \tag{23}$$

Comparing Eqs. (22) and (23), we can know that

$$\overline{w}(\xi) = \frac{2(1-v_s^2)}{E_s}\frac{\overline{q}(\xi)}{\xi[1 + (\frac{s}{l})l\xi + (1 + (\frac{k}{l})^3)l^3\xi^3 + (\frac{g}{l})^2l^5\xi^5]} \tag{24}$$

where

$$l = \sqrt[3]{\frac{2D'(1-v_s^2)}{E_s}}, s = \frac{4\tau_0(1-v_s^2)}{E_s}, k = \sqrt[3]{\frac{(\lambda^s + 2\mu^s)(1-v_s^2)t_f^2}{E_s}} \tag{25}$$

Using Eqs. (24) in (23), we get

$$w(r) = \int_0^{+\infty}\frac{2(1-v_s^2)}{E_s}\frac{\overline{q}(\xi)}{1 + (\frac{s}{l})l\xi + (1 + (\frac{k}{l})^3)l^3\xi^3 + (\frac{g}{l})^2l^5\xi^5}J_0(\xi r)d\xi \tag{26}$$

Letting $t = l\xi$, Eq. (26) can be written as

$$w(r) = \frac{1}{D'^{1/3}}\left(\frac{2(1-v_s^2)}{E_s}\right)^{2/3}\int_0^{+\infty}\frac{\overline{q}(\frac{t}{l})}{1 + (\frac{s}{l})t + (1 + (\frac{k}{l})^3)t^3 + (\frac{g}{l})^2t^5}J_0(\frac{t}{l}r)dt \tag{27}$$

From Eq. (27), it can be seen that once $\overline{q}(t/l)$ is known, the relationship between the film deflection and the indentation load is obtained. To get the specific expression form of $\overline{q}(t/l)$, we assume that the contact stress under the spherical indenter satisfies the Hertz contact. This assumption is reasonable and has been accepted by previous researchers [53]. According to the Hertz contact, $q(r)$ has the form:

$$q(r) = \frac{3Q}{2\pi a^2}[1 - (\frac{r}{a})^2]^{1/2}, r \le a; q(r) = 0, r > a \tag{28}$$

The Hankel transform of Eq. (28) is

$$\overline{q}(\xi) = \frac{3Q}{2\pi a^2}\int_0^a[1 - (\frac{r}{a})^2]^{1/2}J_0(\xi r)rdr \tag{29}$$

Replacing ξ with t/l and using Eqs. (29) in (27), we can get

$$w(r) = \frac{Q}{D'^{1/3}}\left(\frac{2(1-v_s^2)}{E_s}\right)^{2/3}\int_0^{+\infty}\frac{I_1(\alpha, t)}{1 + (\frac{s}{l})t + (1 + (\frac{k}{l})^3)t^3 + (\frac{g}{l})^2t^5}J_0(\frac{t}{l}r)dt \tag{30}$$

where

$$I_1(\alpha, t) = \frac{3}{2\pi\alpha^2}\int_0^\alpha[1 - (\frac{\rho}{\alpha})^2]^{1/2}J_0(t\rho)\rho d\rho; \rho = r/l; \alpha = a/l \tag{31}$$

For the convenience of writing, Eq. (30) can be written as

$$w(r) = I_2(\alpha, \frac{r}{l}) \frac{Q}{D'^{1/3}} [\frac{2(1-v_s^2)}{E_s}]^{2/3}$$
(32)

where

$$I_2(\alpha, \frac{r}{l}) = \int_0^{+\infty} \frac{I_1(\alpha, t)}{1 + (\frac{s}{l})t + (1+(\frac{k}{l})^3)t^3 + (\frac{g}{l})^2 t^5} J_0(t\frac{r}{l}) dt$$
(33)

What needs to be emphasized is that Eq.(32) satisfies all boundary conditions. When r=0, the load-depth relationship is obtained:

$$w(0) = I_2(\alpha, 0) \frac{Q}{D'^{1/3}} [\frac{2(1-v_s^2)}{E_s}]^{2/3}$$
(34)

When the effects of the strain gradient and the surface energy are neglected, Eq. (34) degenerates to the traditional one [18].

2.3. The distribution of bending moment in the film

When E_f/E_s is high, the influence of the contact area on the indentation behaviors of stiff film-compliant substrate structures is small, which will be verified in Section 3. Therefore, to simplify the calculation process of the bending moment in the film, we assume that the indentation load is a concentrated force. Namely, α is equal to zero. At this time, $I_1 = 1/2\pi$. Then, the film deflection can be expressed as

$$w(r) = I_2(\frac{r}{l}) \frac{Q}{2\pi (D')^{1/3}} [\frac{2(1-v_s^2)}{E_s}]^{2/3}$$
(35)

where

$$I_2(\frac{r}{l}) = \int_0^{+\infty} \frac{1}{1 + (\frac{s}{l})t + (1+(\frac{k}{l})^3)t^3 + (\frac{g}{l})^2 t^5} J_0(t\frac{r}{l}) dt$$
(36)

Based on Eqs. (35) and (36), we can know that

$$\frac{dw(r)}{dr} = \frac{Q}{2\pi (D')^{2/3}} [\frac{2(1-v_s^2)}{E_s}]^{1/3} I_3(\frac{r}{l})$$
(37a)

$$\frac{d^2w(r)}{dr^2} = \frac{Q}{2\pi D'} I_4(\frac{r}{l})$$
(37b)

where

$$I_3(\frac{r}{l}) = \int_0^{+\infty} \frac{t}{1 + (\frac{s}{l})t + (1+(\frac{k}{l})^3)t^3 + (\frac{g}{l})^2 t^5} [-J_1(t\frac{r}{l})] dt$$
(38a)

$$I_4(\frac{r}{l}) = \int_0^{+\infty} \frac{t}{1 + (\frac{s}{l})t + (1+(\frac{k}{l})^3)t^3 + (\frac{g}{l})^2 t^5} [\frac{J_1(t\frac{r}{l})}{r/l} - tJ_0(t\frac{r}{l})] dt$$
(38b)

According to the theory of plate, the radial and circumferential bending moments in the film can be written as

$$M_r(r) = -D_{nom}[\frac{d^2w(r)}{dr^2} + v_f \frac{1}{r} \frac{dw(r)}{dr}]; M_\varphi(r) = -D_{nom}[\frac{1}{r} \frac{dw(r)}{dr} + v_f \frac{d^2w(r)}{dr^2}]$$
(39)

where D_{nom} is the nominal bending stiffness of the film, and its definition is illustrated as follows. Eq. (34) can be written in the traditional form:

$$w(0) = I_2^{tra}(\alpha, 0) \frac{Q}{(D_{nom})^{1/3}} [\frac{2(1-v_s^2)}{E_s}]^{2/3}$$
(40)

where I_2^{tra} and D_{nom} read

$$I_2^{tra}(\alpha, 0) = \int_0^{+\infty} \frac{\frac{3}{2\pi\alpha^2} \int_0^\alpha [1-(\frac{\rho}{\alpha})^2]^{1/2} J_0(t\rho)\rho d\rho}{1+t^3} J_0(0) dt$$
(41a)

$$D_{\text{nom}}^{1/3} = \frac{I_2(\alpha, 0)}{I_2^{\text{tra}}(\alpha, 0)} D'^{1/3} \tag{41b}$$

3. Results and discussion

In this section, the influences of the strain gradient and the surface energy on the indentation response of stiff film-compliant substrate structures are analyzed in detail from three aspects: the load-depth relationship, the surface morphology, and the bending moment in the film. For the stiff film-compliant substrate structures used in the MEMS, E_f/E_s is always more than 10^2 and the thickness of the film is usually in the micro or nano scale. Therefore, E_f/E_s changing from 10^3 to 10^5 is studied. The material characteristic length g is usually from 0.1 to 10 μm [54], so we take g/t_f as 0~20. Moreover, the surface energy generally changes from 0.1 to 1 J/m^2. At this time, the surface elastic constant and the surface residual stress are usually -10–10 N/m and 0.1–1 N/m [55], respectively. Hence, we take $(\lambda^s + 2\mu^s)/(E_s t_f)$ and $\tau_0/(E_s t_f)$ as -100–100 and 0–20, respectively. The effects of the strain gradient and the surface energy on the indentation response of stiff film-compliant substrate structures are analyzed as follows.

3.1. The effects of the strain gradient and the surface energy on the load-depth relationship

The load-depth relationship is important data, which is usually used to interpret the indentation data to get the mechanical properties of materials. Therefore, it is significant to investigate the effects of the strain gradient and the surface energy on the load-depth relationship. From Eq. (34), it can be known that $Q/(E_s t_f^2)$ is a function of $w(0)/t_f$, E_f/E_s, v_f, v_s, α, $\lambda^s/(E_s t_f)$, $\mu^s/(E_s t_f)$, $\tau_0/(E_s t_f)$ and g/t_f:

$$\frac{Q}{E_s t_f^2} = f\left(\frac{w(0)}{t_f}, \frac{E_f}{E_s}, v_f, v_s, \alpha, \frac{\lambda^s}{E_s t_f}, \frac{\mu^s}{E_s t_f}, \frac{\tau_0}{E_s t_f}, \frac{g}{t_f}\right) \tag{42}$$

The load-depth relationship at different modulus ratios, characteristic lengths, surface elastic constants, and surface residual stresses are shown in Fig. 2. From Fig. (2), it can be known that the load increases linearly with the increase of the indentation depth. The reason for this is that the bending of the film controls the indentation behavior of the stiff film-compliant substrate structure at this time. However, the slopes are different from each other. As shown in Fig. 2(a), the higher E_f/E_s, the greater the slope. This phenomenon is easy to understand. If we assume that the modulus of the substrate is constant, then the higher the modulus ratio, the larger the modulus of the film. In other words, the higher the modulus ratio, the larger the bending stiffness of the film. The high bending stiffness of the film will lead to great surface settlement when the indenter is pressed into the stiff film-compliant substrate structure, which means that the material of the substrate involving in the deformation also increases. Therefore, under the same indentation depth, the higher the modulus ratio, the greater the slope of the load-depth relationship. Fig. 2(b) shows the results at different material characteristic lengths. It can be known that the slope of the load-depth relationship steeps when g/t_f increases, which is similar to the case where the modulus ratio increases. The reason for this is that the nominal bending stiffness increases with the increase of g/t_f. On the basis of considering the strain gradient, the effects of the surface elastic constant and the surface residual stress on the load-depth relationship are shown in Fig. 2(c) and (d), respectively. It can be seen that the influence of the surface residual stress is significant, but that of the surface elastic constant can be neglected. For example, when w_0/t_f is 0.5, $Q/(E_s t_f^2)$ changes from 17.96 to 18.30 when $(\lambda^s + 2\mu^s)/(E_s t_f)$ is from -100 to 100; however, when $\tau_0/(E_s t_f)$ increases from 0 to 20, $Q/(E_s t_f^2)$ changes from 17.96 to 47.61. Based on the above analysis, we can conclude that when the thickness of the film changes from the macro scale to the nano scale, the indentation behavior will change due to the effects of the strain gradient and the surface energy. More importantly, we find that the dominant factors causing the indentation size effect of the stiff film-compliant substrate structure are the characteristic length and the surface residual stress, and the essence of their effects is to increase the nominal bending stiffness of the film.

3.2. The effects of the strain gradient and the surface energy on the surface morphology

Based on Eq. (32), we can know that $w(r)/t_f$ is a function of r/t_f, E_f/E_s, v_f, v_s, α, $\lambda^s/(E_s t_f)$, $\mu^s/(E_s t_f)$, $\tau_0/(E_s t_f)$ and g/t_f:

$$\frac{w(r)}{t_f} = f\left(\frac{r}{t_f}, \frac{E_f}{E_s}, v_f, v_s, \alpha, \frac{\lambda^s}{E_s t_f}, \frac{\mu^s}{E_s t_f}, \frac{\tau_0}{E_s t_f}, \frac{g}{t_f}\right) \tag{43}$$

Fig. 3 shows the surface morphology of the structure at different modulus ratios, characteristic lengths, surface elastic constants, and surface residual stresses. From Fig. 3(a), it can be seen that the higher the modulus ratio, the smoother the surface. This is because when the modulus of the substrate is assumed to be a constant, the larger the modulus ratio, the greater the bending stiffness of the film. Therefore, under the same indentation depth, the surface settlement range in the case where E_f/E_s is large is greater than that in the case where E_f/E_s is small. When the film thickness changes from the macro scale to the micro/nano scale, the strain gradient and the surface energy begin to affect the shape of the surface morphology. Fig. 3(b) shows that with the increase of g/t_f, the surface becomes smooth, which is similar to the case where
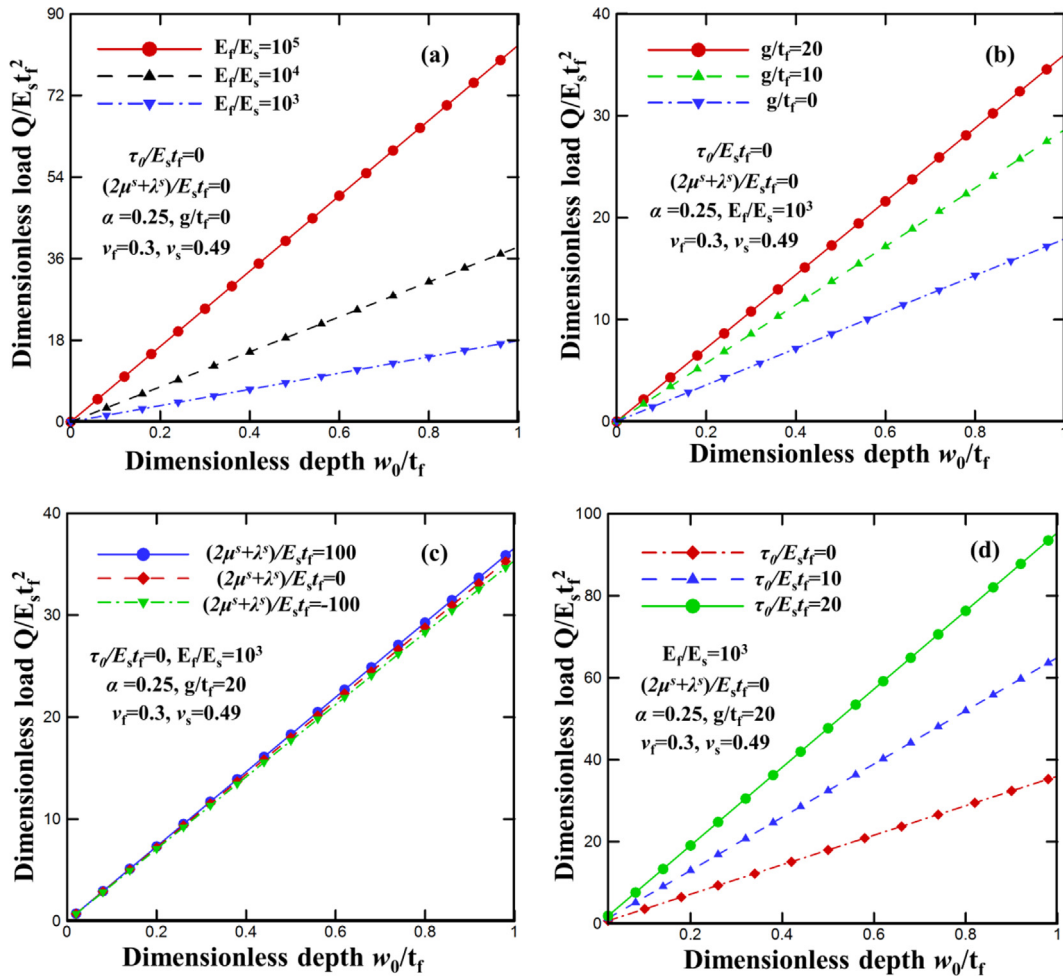
Fig. 2. The load-depth relationship. (a) The effects of strain gradient and surface energy are not considered; (b) only the strain gradient is considered; (c) the effects of strain gradient and surface elastic constant are considered; (d) the effects of strain gradient and surface residual stress are considered.

E_f/E_s increases. On the basis of the strain gradient, the influences of the surface elastic constant and the residual stress on the shape of the surface morphology are further investigated, which are shown in Fig. 3(c) and (d), respectively. As we can see, the effect of surface residual stress on the shape of the surface morphology is significant, but that of the surface elastic constant is small.

3.3. The effects of the strain gradient and the surface energy on the bending moment in the film

The distribution of bending moment in the film is related to its fracture behavior. Therefore, studying the effects of the strain gradient and the surface energy on the distribution of the bending moment is significant. From Eq. (39), it can be known that $M_r/(E_s t_f^2)$ is a function of r/t_f, E_f/E_s, v_f, v_s, α, $\lambda^s/(E_s t_f)$, $\mu^s/(E_s t_f)$, $\tau_0/(E_s t_f)$ and g/t_f:

$$\frac{M_r}{E_s t_f^2} = f(\frac{r}{t_f}, \frac{E_f}{E_s}, v_f, v_s, \alpha, \frac{\lambda^s}{E_s t_f}, \frac{\mu^s}{E_s t_f}, \frac{\tau_0}{E_s t_f}, \frac{g}{t_f}) \tag{44}$$

From Fig. 4(a), it can be seen that the distribution patterns of the radial bending moment are different from each other under different modulus ratios. The maximum radial bending moment in the positive direction, the abscissa of the point where the radial bending moment reaches zero and the maximum, and the maximum bending moment in the negative direction all increase with the increase of the modulus ratio. When the thickness of the film changes from the macro scale to the micro/nano scale, the strain gradient and surface energy begin to influence the distribution pattern of the radial bending moment. However, their influences on the distribution pattern of the radial bending moment are similar to, but not identical to, that of the modulus ratio. As shown in Fig. 4(b), when the strain gradient is considered, the maximum bending moment in the positive direction first decreases and then increases with the increase of g/t_f. For example, when g/t_f changes from 0 to 10, the dimensionless maximum bending moment changes from 6.88 to 3.12; and when g/t_f changes
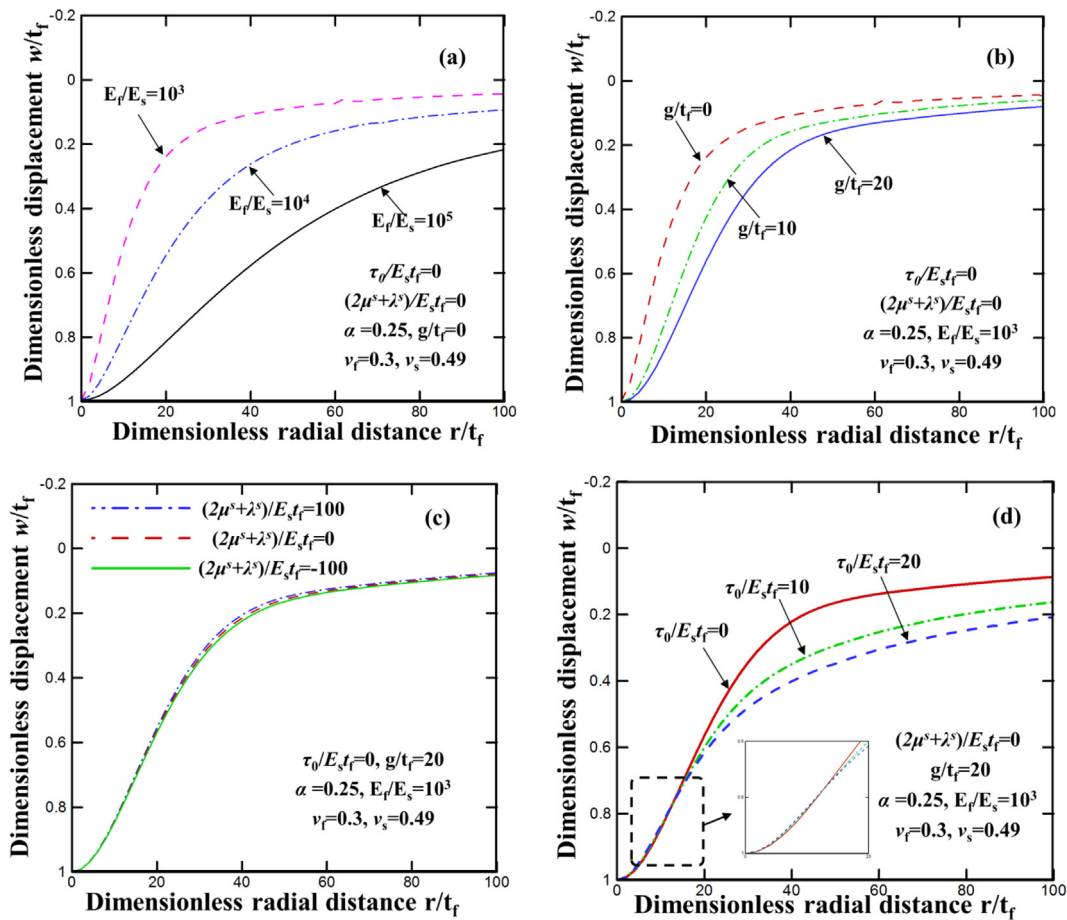
Fig. 3. The surface topography. (a) The effects of strain gradient and surface energy are not considered; (b) only the strain gradient is considered; (c) the effects of strain gradient and surface elastic constant are considered; (d) the effects of strain gradient and surface residual stress are considered.

from 10 to 20, the dimensionless maximum bending moment changes from 3.12 to 3.72. In addition, when g/t_f increases, the maximum bending moment in the negative direction increases, and the abscissa of the point where the bending moment reaches the maximum in the negative direction and zero becomes large. On the basis of considering the strain gradient, the influences of the surface elastic constant and the surface residual stress on the distribution pattern of the radial bending moment are studied, which are shown in Fig. 4(c) and (d), respectively. From the figures, we can know that the effect of the surface residual stress on the radial bending moment is significant, and that of the surface elastic constant can be neglected. Moreover, the effect of the residual stress on the distribution pattern of the radial bending moment is different from that of the strain gradient. For example, when $\tau_0/(E_s t_f)$ changes from 0 to 20, the maximum bending moments in the positive and negative direction increase, but the abscissa of the point where the bending moment reaches the maximum and zero does not change significantly.

Different from the distribution pattern of the radial bending moment, the circumferential bending moment decreases with the increase of the radial distance monotonically. As shown in Fig. 5(a), when the modulus ratio increases, the maximum circumferential bending moment becomes large, and the abscissa of the point where the circumferential bending moment decreases to zero increases. In addition, the distribution patterns of the circumferential bending moment at different modulus ratios are similar to each other. However, when the strain gradient and the surface energy are considered, there is no similarity in the distribution patterns of the circumferential bending moment. As shown in Fig. 5(b), when g/t_f increases from 0 to 20, the maximum circumferential bending moment first decreases and then increases, and the abscissa of the point where the circumferential bending moment decreases to zero increases. In addition, based on Fig. 5(c) and (d), we find that the surface elastic constant has little influence on the distribution patterns of the circumferential bending moment, but the influence of the surface residual stress is significant. For example, from Fig. 5(d), it can be seen that the maximum circumferential bending moment increases sharply when $\tau_0/(E_s t_f)$ increases from 0 to 20.

Based on the above analysis, it can be known that when the thickness of the film changes from the macro scale to the micro/nano scale, the indentation behavior of the structure will change significantly due to the effects of the strain gradient and the surface residual stress. The essence of their effects on the indentation response is to increase the nominal bending
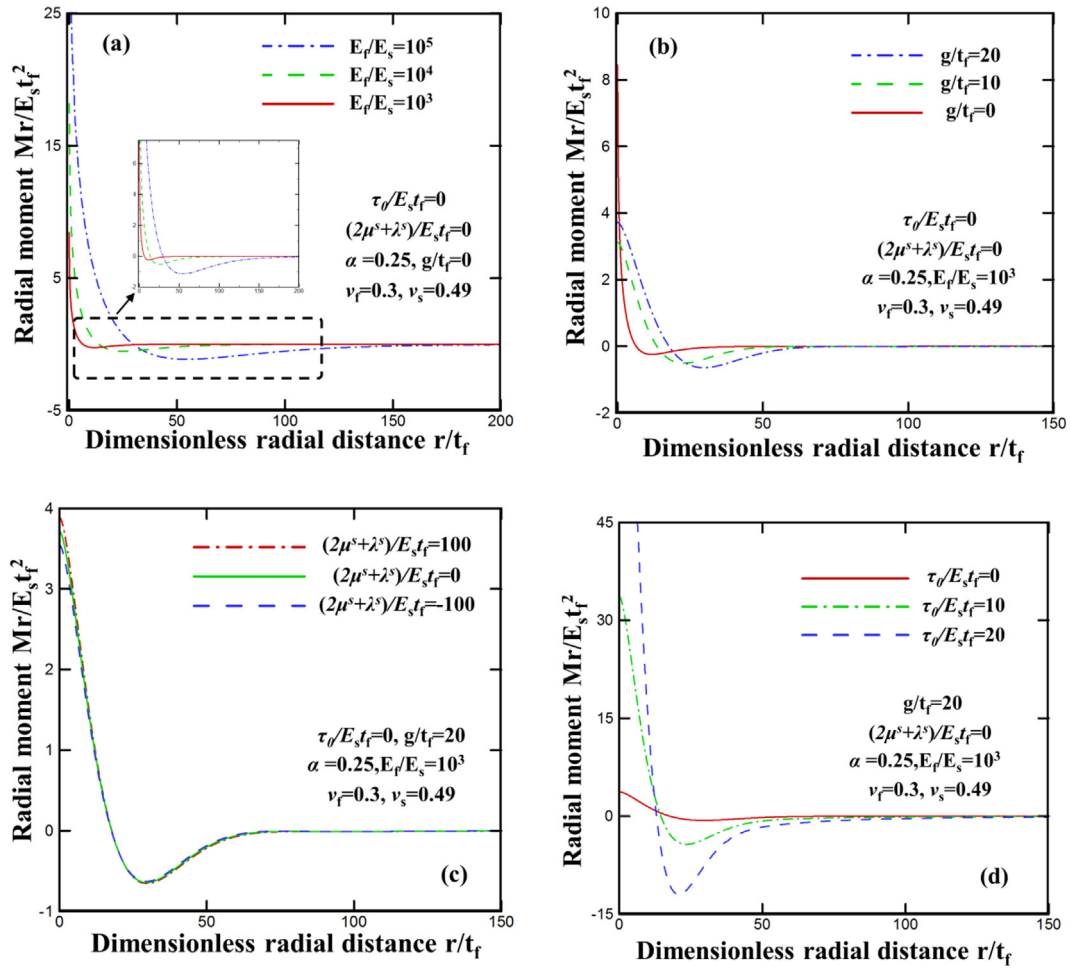
Fig. 4. The radial bending moment. (a) The effects of strain gradient and surface energy are not considered; (b) only the strain gradient is considered; (c) the effects of strain gradient and surface elastic constant are considered; (d) the effects of strain gradient and surface residual stress are considered.

stiffness of the film, which is similar to, but not identical to, that of the modulus ratio. In addition, what needs to be added is that the effect of the surface elastic constant can be neglected.

4. Analysis of factors influencing the size effect of indentation behavior of the stiff film-compliant substrate structure

In Section 3, the influence of strain gradient and surface energy on the indentation response is focused on, and we found that there is a strong size effect in the indentation response of stiff film-compliant substrate structures. At this time, we will ask the question that whether the indentation size effect is influenced by other factors, such as the modulus ratio, the contact area, and Poisson's ratio. In this section, their influences on the indentation size effect are investigated.

For the stiff film-compliant substrate structure used in MEMS and scientific research, it can be known that the range of E_f/E_s is from 10^3 to 10^5, and the Poisson's ratio is usually from 0.2 to 0.49. So we focus on this range. In addition, previous research has stated that there will be an obvious sink-down phenomenon when the indenter is pressed into the stiff film-compliant substrate structure [56], so α is usually smaller than 0.5. Here, we take α as 0.1–0.25. Fig. 6 shows the influences of modulus ratio, Poisson's ratio and contact radius on the indentation size effect. As we can see, due to the influences of the strain gradient and the surface energy, the nominal bending stiffness increases with the decrease of the film thickness. However, under different modulus ratios, the indentation size effect is different from each other. From Fig. 6(a), it can be known that at the same film thickness, the higher the modulus ratio, the smaller the nominal bending stiffness. In other words, the high modulus ratio will inhibit the indentation size effect caused by the strain gradient and the surface energy. In addition, from Fig. 6(b) and (c), we can know that the indentation size effect is not sensitive to the Poisson's ratio and the contact radius.

From Section 3, we know that the main factors leading to the indentation size effect are the characteristic length, g, and the surface residual stress, τ_0. The influence of the surface elastic constants can be neglected. In addition, according to
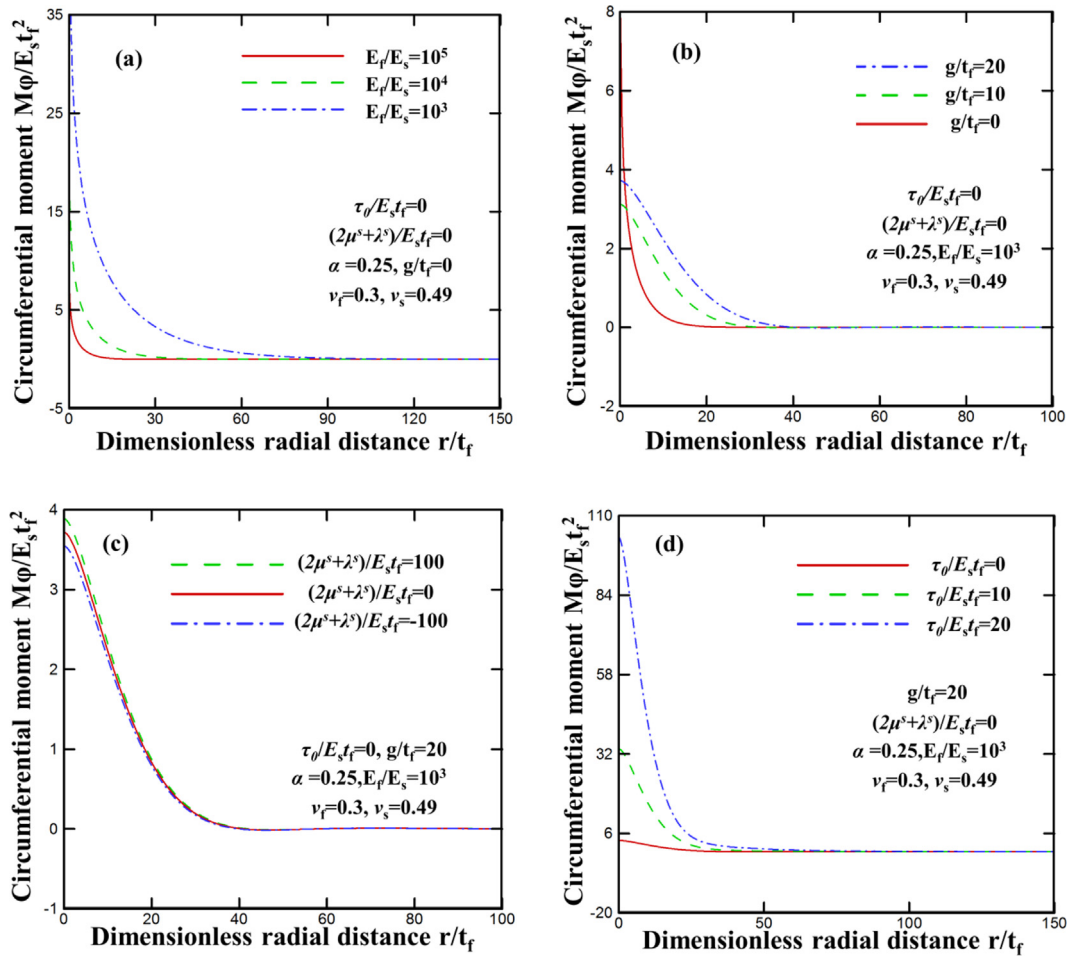
Fig. 5. The circumferential bending moment. (a) The effects of strain gradient and surface energy are not considered; (b) only the strain gradient is considered; (c) the effects of strain gradient and surface elastic constant are considered; (d) the effects of strain gradient and surface residual stress are considered.

the analysis of this Section, we find that the indentation size effect caused by the strain gradient and the surface energy is sensitive to the modulus ratio of the film to the substrate but has little relation with the Poisson's ratio and the contact radius. Combining the above findings and Eq. (32), it is exciting to find that two dimensionless numbers, $g/(E_s^{-1/3}E_f^{1/3}t_f)$ and $\tau_0/(E_s^{2/3}E_f^{1/3}t_f)$, control the indentation size effect of the stiff film-compliant substrate structure. Then, we draw the control surface of the indentation size effect in the space composed of $g/(E_s^{-1/3}E_f^{1/3}t_f)$, $\tau_0/(E_s^{2/3}E_f^{1/3}t_f)$ and D_{nor}/D_f, which is shown in Fig. 7. From Fig. 7, we can know that when the film thickness decreases from the macro scale to the micro scale, the indentation size effect is mainly controlled by $g/(E_s^{-1/3}E_f^{1/3}t_f)$. For example, when the film thickness is 1 μm and the modulus ratio is 10^3, according to the common range of the characteristic length and the surface residual stress, $\tau_0/(E_s^{2/3}E_f^{1/3}t_f)$ is 0.01–0.1 and $g/(E_s^{-1/3}E_f^{1/3}t_f)$ is 0.1–1. At this time, the influence of the surface residual stress is small. Therefore, when the film thickness is at the micro scale, the indentation size effect is mainly caused by the strain gradient. When the film thickness continues to decrease, the effect of the surface residual stress becomes more and more significant. For example, when the film thickness is 50 nm and the modulus ratio is 10^3, $\tau_0/(E_s^{2/3}E_f^{1/3}t_f)$ is 0.2–2 and $g/(E_s^{-1/3}E_f^{1/3}t_f)$ is 2–20. At this time, as shown in Fig. 7, the influence of the surface residual stress cannot be neglected. Namely, when the film thickness is at the nano scale, the indentation size effect depends on both the strain gradient and the surface residual stress.

5. Experiment

In this section, the experiment is conducted to validate the effectiveness of the MSI model. Cu/PDMS layered structure as a typical stiff film-compliant substrate structure is used as the experimental sample. In this section, firstly, the preparation and characterization of the samples are introduced in detail; then, the normalized bending stiffness of the Cu nanofilm measured by the indentation test is compared with that predicted by the MSI model.
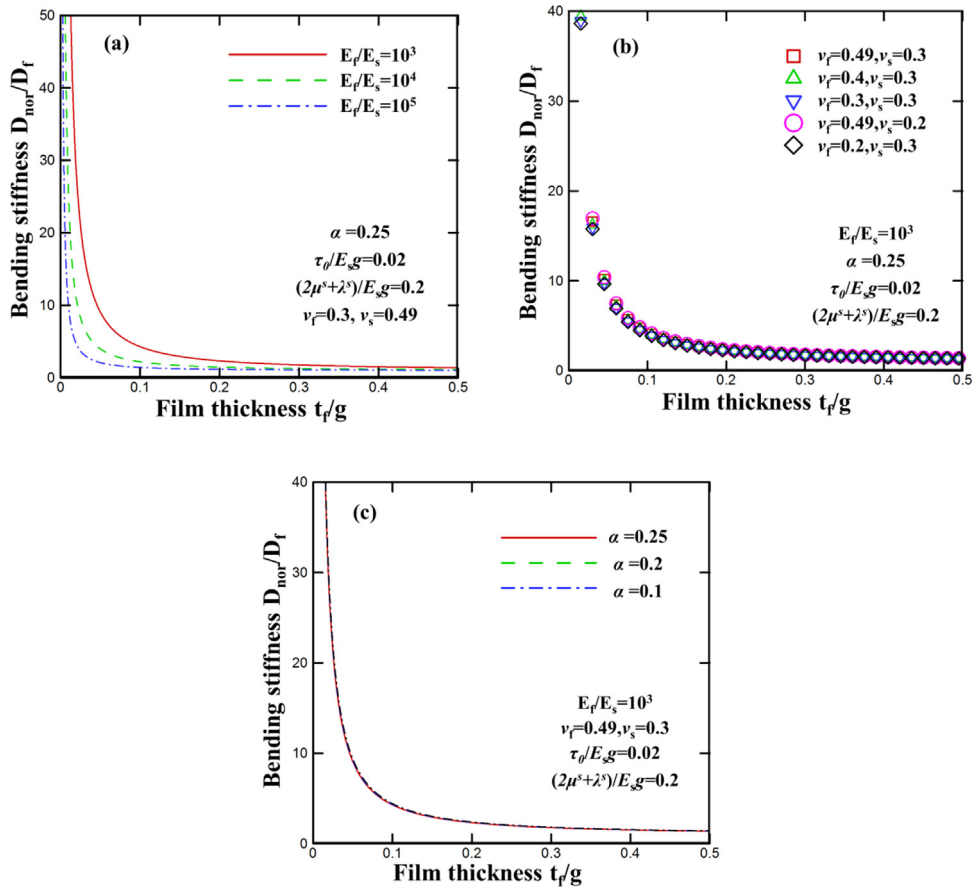
Fig. 6. The relationship between the nominal bending stiffness and film thickness. (a) The results at different modulus ratios; (b) the results at different Poisson's ratios; (c) the results at different contact radii.
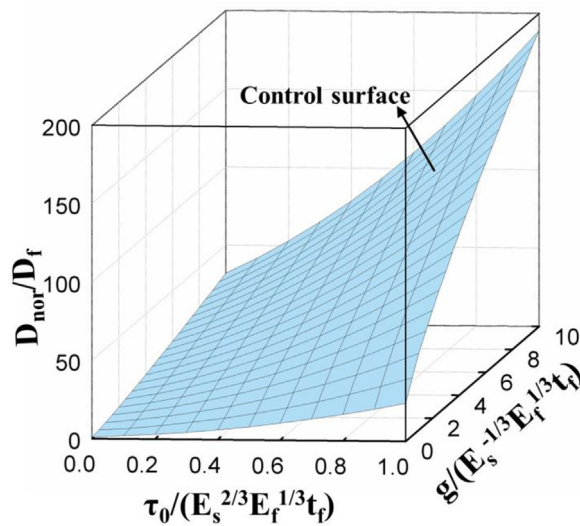

Fig. 7. The relationship between the normalized bending stiffness and the dimensionless numbers proposed by us.
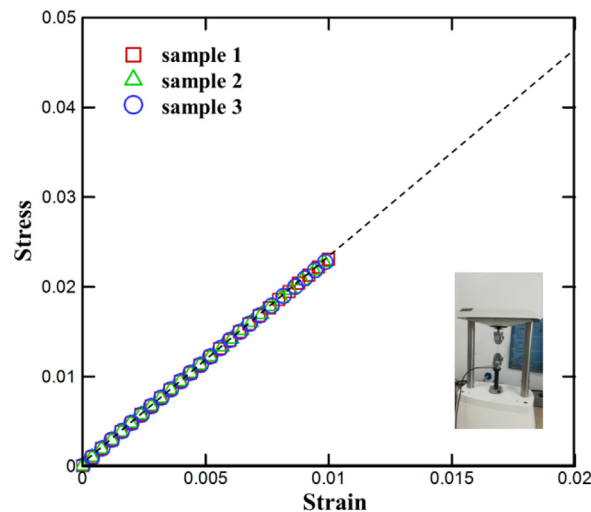
Fig. 8. The stress-strain relationship of PDMS.

5.1. Sample preparation and characterization

Preparation and characterization of PDMS: Sylgard 184, which is produced by Dow Corning (USA), is used to prepare PDMS. Mixing the main agent and the curing agent with a ratio of 10:1, and curing the mixture at 85 °C for 4 h, then the PDMS with a thickness of 3 mm is obtained. The modulus of PDMS is measured as 2.319±0.036 MPa by the ElectroForce 3100 test instrument produced by the American BOSE company, and the stress-strain relationship of PDMS is shown in Fig. 8.

Preparation and characterization of Cu/PDMS: High Vacuum Magnetron Sputtering Coating Machine (PVD75120303) produced by Kurt J. Lesker is used to coat the PDMS wafer sized 1 cm × 1 cm with a Cu nanofilm (purity of the Cu: 99.999%). There are three Cu/PDMS samples with different thicknesses of Cu nanofilm, and they are shown in Fig. 9. Then, the indentation test is conducted by an *in-situ* nanomechanical test system (TI-900 TriboIndenter). A Berkovich indenter with a tip radius of 50 nm is used, and the tests are conducted at room temperature (-18 °C). The maximum indentation depth is less than the thickness of the Cu nanofilm, and every sample is tested by 5–8 times. The indentation load-depth relationship is shown in Fig. 10. Based on the method proposed by us [18], the normalized bending stiffness of the Cu nanofilm can be calculated, which will be compared with that predicted by the MSI model.

Thickness characterization of Cu nanofilm: When the Cu is coated on the top of the PDMS, a half-covered silicon wafer is also placed in the chamber of the High Vacuum Magnetron Sputtering Coating Machine. Then, the thickness of the Cu nanofilm coated on the half-covered silicon wafer is measured by atomic force microscopy (AFM, Brucker Corporation, Multimode 8 SPM), which is shown in Fig. 9. The measured thickness of the Cu nanofilm is taken as the thickness of the Cu nanofilm on the PDMS. The thicknesses of the Cu nanofilm of the three samples are measured as 130, 71.8, and 39.5 nm, respectively.

5.2. Results and discussion

The load-displacement relationship is the first-hand and the most important data of the indentation experiment, and it is always used to obtain the mechanical properties of the materials. As shown in Fig. 10, the indentation load linearly increases with the increase of the indentation depth. The reason for this is as follows. For the indentation response of the stiff film-compliant substrate structure, the indentation deformation can be divided into two parts: one is the settlement of the compliant substrate, and the other is the deflection of the film. Although the indentation depth is comparable to the film thickness, the film deflection is still small. Therefore, the linear relationship occurs when the indentation depth is less than the film thickness, which has been verified by our previous work [18]. In addition, the data of the loading is in good agreement with that of the unloading, which shows that the system is elastically deformed. That is, there is no slip at the interface between the Cu nanofilm and the PDMS. By fitting the data, we can get the slope of the load-depth relationship. Then, based on our previous work [18], the normalized bending stiffness can be calculated. Here, the Poisson's ratios of Cu and PDMS are 0.35 and 0.49, respectively. According to previous research, the modulus of Cu is about 118–126 GPa [57–59], so we take the modulus of Cu as 123 GPa in the calculation.

The load-depth relationship predicted by the MSI model is also plotted in Fig. 10. The predicted results of the MSI model are different from the fitting results. However, as shown in Fig. 11, the MSI model is more consistent with the experimental results compared with the SG model. From the experiment results in this figure, it can be seen that the normalized bending stiffness of the Cu film exhibits a strong size effect. Namely, with the decrease in the thickness of
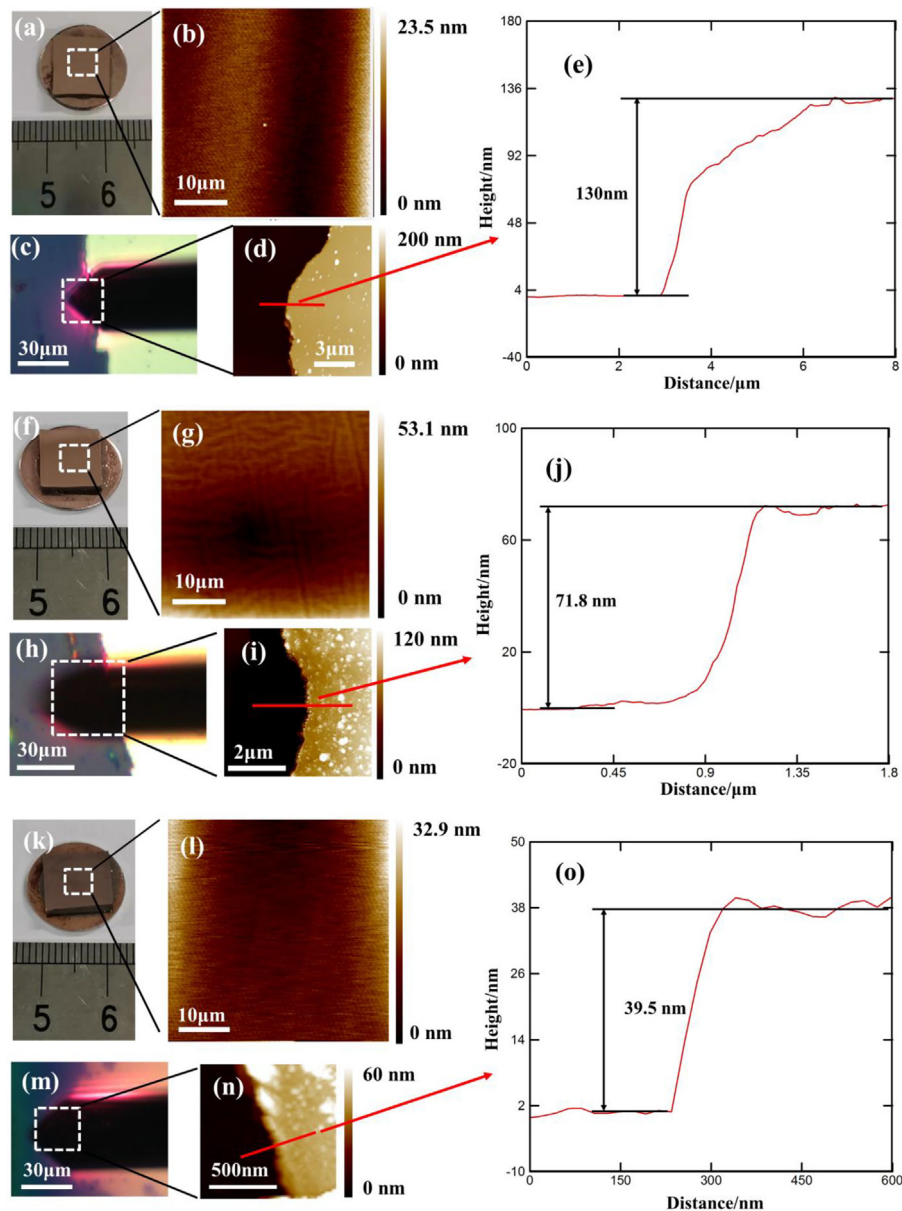
Fig. 9. (a) the photograph of the Cu/PDMS sample 1; (b) AFM image of the central region of the Cu/PDMS sample 1; (c) the optical image of Cu/Si sample 1; (d) AFM image of the central region of the Cu/Si sample 1; (e) the measurement result of the thickness of Cu nanofilm of sample 1; (f) the photograph of the Cu/PDMS sample 2; (g) AFM image of the central region of the Cu/PDMS sample 2; (h) the optical image of Cu/Si sample 2; (i) AFM image of the central region of the Cu/Si sample 2; (j) the measurement result of the thickness of Cu nanofilm of sample 2; (k) the photograph of the Cu/PDMS sample 3; (l) AFM image of the central region of the Cu/PDMS sample 3; (m) the optical image of Cu/Si sample 3; (n) AFM image of the central region of the Cu/Si sample 3; (o) the measurement result of the thickness of Cu nanofilm of sample 3.

the Cu nanofilm, the normalized bending stiffness of the film increases, significantly. To verify the effectiveness of the MSI model, the predicted normalized bending stiffness of Cu film mounted on PDMS is compared with the experimental result. The method of comparing the normalized bending stiffness to explain the effects of the strain gradient and the surface energy was widely adopted by previous researchers [25]. According to previous work, the characteristic length of Cu is 0.5–5 μm [60]. In this paper, we take it as 2.5 μm. Based on the molecular simulation, the previous research shows that the surface elastic modulus of Cu is -10–5 N/m, and the surface residual stress of Cu is 0–1 N/m [55]. Here, we take the surface elastic modulus and the surface residual stress of Cu as -1 and 0.5 N/m, respectively. The predicted normalized bending stiffness of Cu film coated on the PDMS by the SG model and MSI model is shown in Fig. 11. Based on the indentation experiment of Cu/PDMS, we find that the SG model is suitable only when the film thickness is greater than 100 nm. When the film thickness is less than 100 nm, the SG model will underestimate the normalized bending stiffness of the film. For
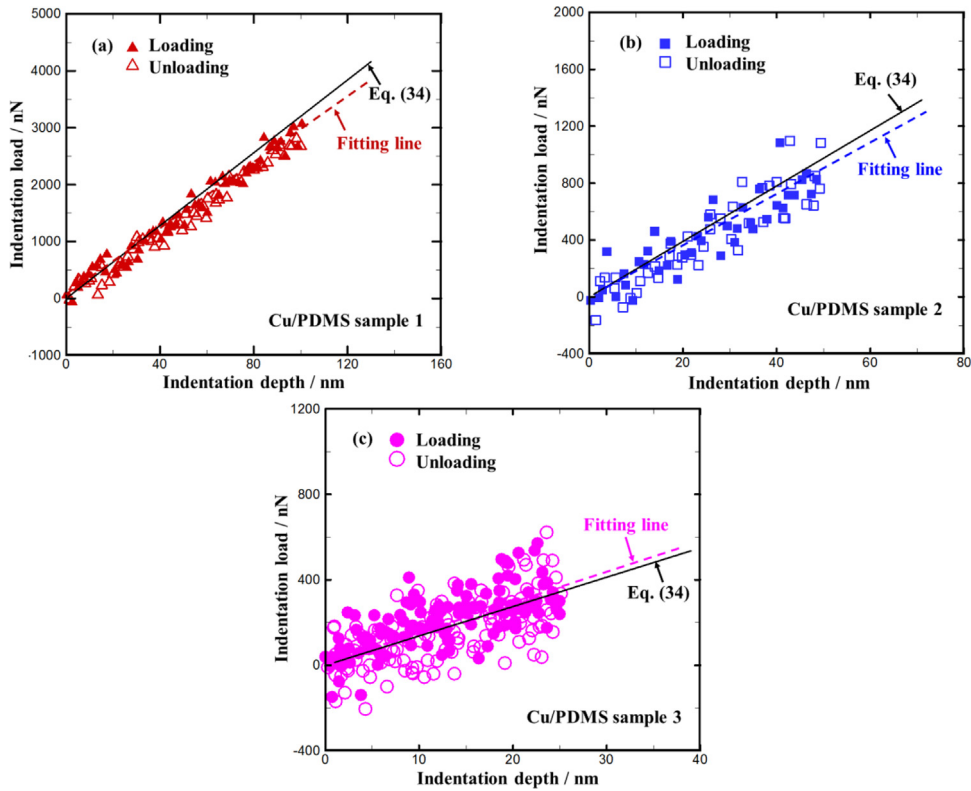
Fig. 10. The relationship between the indentation load and indentation depth. (a) The results of sample 1, the thickness of Cu nanofilm is 130 nm; (b) the results of sample 2, the thickness of Cu nanofilm is 71.8 nm; (c) the results of sample 3, the thickness of Cu nanofilm is 39.5 nm.
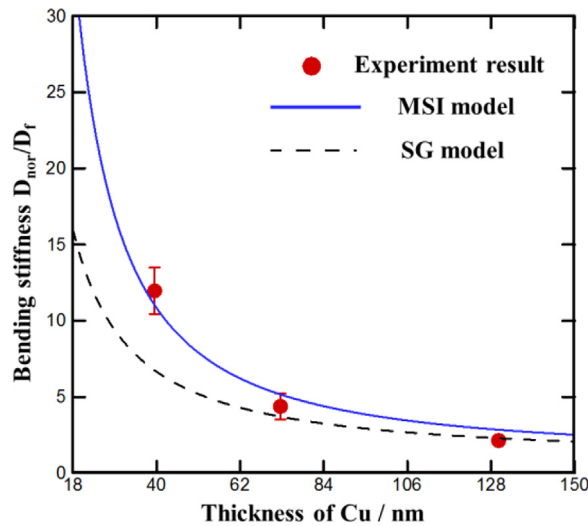

Fig. 11. The relationship between the normalized bending stiffness and the thickness of the Cu nanofilm. The symbol is for the experiment, the solid line is for the MSI model, and the dashed line is for the SG model.

example, when the thickness of the Cu film is 71.8 and 39.5 nm, the difference between the SG model and the experiment is 18.4% and 77.6%. This is because the effect of the surface energy is not considered in the SG model. Compared with the SG model [32], the predicted normalized bending stiffness of Cu film coated on the PDMS by the MSI model is in better agreement with the experiment result when the film thickness is less than 100 nm. For example, when the thickness of the Cu film is 71.8 and 39.5 nm, the difference between the MSI model and the experiment is 14.9% and 9.2%, which verifies the effectiveness of the MSI model. It should be noted that this paper only preliminarily verified the effectiveness of the model.

In future work, more experimental data are needed to verify the effectiveness of the model and evaluate the applicable scope of the model.

6. Conclusion remarks

In this work, the multi-scale indentation response of stiff film-compliant substrate structures is studied based on the theory and the experiment. Firstly, based on the strain gradient theory and the surface elastic model, the MSI model for the stiff film-compliant substrate structure is derived with the Hankel transform. Then, with this model, the indentation size effect is investigated in detail. The results show that with the decrease of the film thickness, the influences of the strain gradient and the surface energy on the indentation response of the stiff film-compliant substrate structure become more and more significant. When the film thickness decreases from the macro scale to the micro scale, the strain gradient first begins to affect the indentation response. At this scale, the indentation size effect is mainly caused by the strain gradient. As the film thickness is further reduced from the micro scale to the nano scale, the influence of the surface energy becomes more and more obvious. It should be emphasized that the surface residual stress is the main factor affecting the indentation response, and the influence of the surface elastic modulus can be neglected. At this scale, the indentation size effect is caused by the strain gradient and the surface residual stress. In addition, the factors influencing the indentation size effect are investigated. We find that the indentation size effect caused by the strain gradient and the surface energy is sensitive to E_f/E_s, but has little relationship with the contact radius and the Poisson's ratio. The high modulus ratio will inhibit the indentation size effect. Based on the above analysis, two dimensionless numbers $g/(E_s^{-1/3}E_f^{1/3}t_f)$ and $\tau_0/(E_s^{2/3}E_f^{1/3}t_f)$ are proposed to evaluate the indentation size effect. Finally, the indentation experiment of the Cu/PDMS layered structure is carried out to validate the effectiveness of the MSI model. The results show that when the thickness of the Cu decreases from 130 to 39.5 nm, the nominal bending stiffness increases from 2.14 to 11.96. The bending stiffness of the film predicted by the MSI model is consistent with the experimental result, which verifies the effectiveness of the MSI model. Our research sheds light on the understanding of the indentation size effect of the stiff film-compliant substrate structure and provides theoretical guidance for the design of related devices.

Data availability

Data will be made available on request.

Acknowledgment

Appendix A. The derivation of Eq. (5)

Dividing Eq. (4) into two parts, we have

$$U_1^{tra} = \frac{1}{2} \iiint \sigma_{xx}\varepsilon_{xx} + \sigma_{yy}\varepsilon_{yy} + 2\sigma_{xy}\varepsilon_{xy} dxdydz \tag{A.1}$$

$$U_1^{gra} = \frac{1}{2} \iiint \tau_{xxx}\varepsilon_{xx,x} + 2\tau_{xyx}\varepsilon_{xy,x} + \tau_{yyx}\varepsilon_{yy,x} + \tau_{xxy}\varepsilon_{xx,y} + 2\tau_{xyy}\varepsilon_{xy,y} + \tau_{yyy}\varepsilon_{yy,y} dxdydz \tag{A.2}$$

Using Eqs. (1) and (3) in Eq. (A.1), we can get

$$U_1^{tra} = \frac{1}{2}D \iint_A \left(\frac{\partial^2 w}{\partial x^2}\right)^2 + \left(\frac{\partial^2 w}{\partial y^2}\right)^2 + 2\left(\frac{\partial^2 w}{\partial x \partial y}\right)^2 + 2v_f\left(\frac{\partial^2 w}{\partial x^2}\frac{\partial^2 w}{\partial y^2} - \left(\frac{\partial^2 w}{\partial x \partial y}\right)^2\right) dxdy \tag{A.3}$$

There are many terms in Eq. (A.3). Here, taking the first term as an example, the specific solution process of variation is given as follows:

$$
\begin{aligned}
\frac{1}{2}D\delta\left(\iint_A \left(\frac{\partial^2 w}{\partial x^2}\right)^2 dxdy\right) &= D\iint_A \frac{\partial^2 w}{\partial x^2}\frac{\partial^2 \delta w}{\partial x^2} dxdy \\
&= D\iint_A \frac{\partial}{\partial x}\left(\frac{\partial^2 w}{\partial x^2}\frac{\partial \delta w}{\partial x}\right) - \frac{\partial}{\partial x}\left(\frac{\partial^3 w}{\partial x^3}\delta w\right) + \frac{\partial^4 w}{\partial x^4}\delta w dxdy \\
&= D\iint_A \frac{\partial^4 w}{\partial x^4}\delta w dxdy + D\int_S \frac{\partial^2 w}{\partial x^2}\frac{\partial \delta w}{\partial x} dy - D\int_S \frac{\partial^3 w}{\partial x^3}\delta w dy \\
&= D\iint_A \frac{\partial^4 w}{\partial x^4}\delta w dxdy + D\int_S \frac{\partial^2 w}{\partial x^2}\left(\frac{\partial \delta w}{\partial n}\cos\alpha - \frac{\partial \delta w}{\partial s}\sin\alpha\right)\cos\alpha ds \\
&\quad - D\int_S \frac{\partial^3 w}{\partial x^3}\delta w \cos\alpha ds \\
&= D\iint_A \frac{\partial^4 w}{\partial x^4}\delta w dxdy + D\int_S \frac{\partial^2 w}{\partial x^2}\cos^2\alpha\frac{\partial \delta w}{\partial n} ds \\
&\quad + D\int_S \frac{\partial}{\partial s}\left(\frac{\partial^2 w}{\partial x^2}\sin\alpha\cos\alpha\right)\delta w ds - D\int_S \frac{\partial^3 w}{\partial x^3}\cos\alpha\delta w ds
\end{aligned}
\tag{A.4}
$$

The same method is used for the other terms, and one has

$$
\begin{aligned}
\delta U_1^{tra} &= D\iint_A \nabla^4 w\delta w dxdy + D\int_S [(\tfrac{\partial^2 w}{\partial x^2} + \nu_f \tfrac{\partial^2 w}{\partial y^2})\cos^2\alpha \\
&+ (\tfrac{\partial^2 w}{\partial y^2} + \nu_f \tfrac{\partial^2 w}{\partial x^2})\sin^2\alpha + 2(1-\nu_f)\tfrac{\partial^2 w}{\partial x\partial y}\sin\alpha\cos\alpha]\tfrac{\partial\delta w}{\partial n}ds \\
&+ D\int_S [-(\tfrac{\partial^3 w}{\partial x^3} + \tfrac{\partial^3 w}{\partial x\partial y^2})\cos\alpha - (\tfrac{\partial^3 w}{\partial y^3} + \tfrac{\partial^3 w}{\partial y\partial x^2})\sin\alpha \\
&+ (1-\nu)\tfrac{\partial}{\partial s}((\tfrac{\partial^2 w}{\partial x^2} - \tfrac{\partial^2 w}{\partial y^2})\sin\alpha\cos\alpha + \tfrac{\partial^2 w}{\partial x\partial y}(\sin^2\alpha - \cos^2\alpha))]\delta wds
\end{aligned}
\tag{A.5}
$$

Using Eqs. (1) and (3) in Eq. (A.2), we can get

$$
\begin{aligned}
U_1^{gra} &= \tfrac{1}{2}g^2 D\iint_A (\tfrac{\partial^3 w}{\partial x^3})^2 + (\tfrac{\partial^3 w}{\partial y^3})^2 + 3[(\tfrac{\partial^3 w}{\partial x\partial y^2})^2 + (\tfrac{\partial^3 w}{\partial y\partial x^2})^2] \\
&+ 2\nu_f[\tfrac{\partial^3 w}{\partial x\partial y^2}\tfrac{\partial^3 w}{\partial x^3} + \tfrac{\partial^3 w}{\partial y\partial x^2}\tfrac{\partial^3 w}{\partial y^3} - (\tfrac{\partial^3 w}{\partial x\partial y^2})^2 - (\tfrac{\partial^3 w}{\partial y\partial x^2})^2]dxdy
\end{aligned}
\tag{A.6}
$$

Performing variational calculation on Eq. (A.6), one has

$$
\begin{aligned}
\delta U_1^{gra} &= -g^2 D\iint_A \nabla^6 w\delta w dxdy \\
&+ g^2 D\int_S 2\tfrac{\partial}{\partial s}(\tfrac{\partial^3 w}{\partial x^3}\sin\alpha\cos^2\alpha) - \tfrac{\partial^4 w}{\partial x^4}\cos^2\alpha - 2\tfrac{\partial}{\partial s}(\tfrac{\partial^3 w}{\partial y^3}\cos\alpha\sin^2\alpha) \\
&- \tfrac{\partial^4 w}{\partial y^4}\cos^2\alpha - 3\tfrac{\partial^4 w}{\partial x^2\partial y^2}\sin^2\alpha - 6\tfrac{\partial}{\partial s}(\tfrac{\partial^3 w}{\partial x\partial y^2}\sin\alpha\cos^2\alpha) \\
&- 3\tfrac{\partial^4 w}{\partial x^2\partial y^2}\cos^2\alpha + 6\tfrac{\partial}{\partial s}(\tfrac{\partial^3 w}{\partial x^2\partial y}\cos\alpha\sin^2\alpha) \\
&- \nu_f\tfrac{\partial}{\partial s}[(\cos^2\alpha - \sin^2\alpha)(\cos\alpha(\tfrac{\partial^3 w}{\partial y^3} - \tfrac{\partial^3 w}{\partial x^2\partial y}) - \sin\alpha(\tfrac{\partial^3 w}{\partial x\partial y^2} - \tfrac{\partial^3 w}{\partial x^3})) \\
&+ 4\sin\alpha\cos\alpha(\tfrac{\partial^3 w}{\partial x^2\partial y}\sin\alpha - \tfrac{\partial^3 w}{\partial x\partial y^2}\cos\alpha)]\tfrac{\partial\delta w}{\partial n}ds \\
&+ g^2 D\int_S [\tfrac{\partial^3 w}{\partial x^3}\cos^3\alpha + \tfrac{\partial^3 w}{\partial y^3}\sin^3\alpha + 3\tfrac{\partial^3 w}{\partial x\partial y^2}\sin^2\alpha\cos\alpha \\
&+ 3\tfrac{\partial^3 w}{\partial x^2\partial y}\cos^2\alpha\sin\alpha + \nu_f(\cos^2\alpha - \sin^2\alpha)(\tfrac{\partial^3 w}{\partial x\partial y^2}\cos\alpha - \tfrac{\partial^3 w}{\partial x^2\partial y}\sin\alpha) \\
&+ \nu_f\cos\alpha\sin\alpha(\cos\alpha(\tfrac{\partial^3 w}{\partial y^3} - \tfrac{\partial^3 w}{\partial x^2\partial y}) - \sin\alpha(\tfrac{\partial^3 w}{\partial x\partial y^2} - \tfrac{\partial^3 w}{\partial x^3}))]\tfrac{\partial^2\delta w}{\partial n^2}ds \\
&+ g^2 D\int_S [\tfrac{\partial^2}{\partial s^2}(\tfrac{\partial^3 w}{\partial x^3}\cos\alpha\sin^2\alpha) - \tfrac{\partial}{\partial s}(\tfrac{\partial^4 w}{\partial x^4}\cos\alpha\sin\alpha) + \tfrac{\partial^5 w}{\partial x^5}\cos\alpha \\
&+ \tfrac{\partial^2}{\partial s^2}(\tfrac{\partial^3 w}{\partial y^3}\cos^2\alpha\sin\alpha) + \tfrac{\partial}{\partial s}(\tfrac{\partial^4 w}{\partial y^4}\cos\alpha\sin\alpha) + \tfrac{\partial^5 w}{\partial y^5}\sin\alpha \\
&+ 3\tfrac{\partial^2}{\partial s^2}(\tfrac{\partial^3 w}{\partial x\partial y^2}\cos^3\alpha) + 3\tfrac{\partial}{\partial s}(\tfrac{\partial^4 w}{\partial x^2\partial y^2}\cos\alpha\sin\alpha) + 3\tfrac{\partial^5 w}{\partial x^2\partial y^3}\sin\alpha \\
&+ 3\tfrac{\partial^2}{\partial s^2}(\tfrac{\partial^3 w}{\partial x^2\partial y}\sin^3\alpha) + 3\tfrac{\partial^5 w}{\partial y^2\partial x^3}\cos\alpha - 3\tfrac{\partial}{\partial s}(\tfrac{\partial^4 w}{\partial x^2\partial y^2}\cos\alpha\sin\alpha) \\
&- \tfrac{\partial^2}{\partial s^2}[(\cos^2\alpha - \sin^2\alpha)(\tfrac{\partial^3 w}{\partial x\partial y^2}\cos\alpha - \tfrac{\partial^3 w}{\partial x^2\partial y}\sin\alpha) \\
&+ \sin\alpha\cos\alpha(\cos\alpha(\tfrac{\partial^3 w}{\partial y^3} - \tfrac{\partial^3 w}{\partial y\partial x^2}) - \sin\alpha(\tfrac{\partial^3 w}{\partial x\partial y^2} - \tfrac{\partial^3 w}{\partial x^3}))]\delta wds
\end{aligned}
\tag{A.7}
$$

Then δU_1 can be expressed as

$$
\begin{aligned}
\delta U_1 &= \delta U_1^{tra} + \delta U_1^{gra} \\
&= \iint_A (D\nabla^4 w - g^2 D\nabla^6 w)\delta w dxdy \\
&+ \int_S (D\Xi_1 + g^2 D\Xi_2)\tfrac{\partial\delta w}{\partial n}ds + \int_S g^2 D\Xi_3 \tfrac{\partial^2\delta w}{\partial n^2}ds + \int_S (D\Theta_1 + g^2 D\Theta_2)\delta wds
\end{aligned}
\tag{A.7}
$$

Appendix B. The derivation of Eq. (11)

The variation of the elastic strain energy of the film surface is

$$
\begin{aligned}
\delta U_2 &= \iint \tfrac{(\lambda^s + 2\mu^s)t_f^2}{4}[2\tfrac{\partial^2 w}{\partial x^2}\tfrac{\partial^2\delta w}{\partial x^2} + 2\tfrac{\partial^2 w}{\partial y^2}\tfrac{\partial^2\delta w}{\partial y^2} + 2(\tfrac{\partial^2 w}{\partial x^2}\tfrac{\partial^2\delta w}{\partial y^2} + \tfrac{\partial^2 w}{\partial y^2}\tfrac{\partial^2\delta w}{\partial x^2})] \\
&- \tfrac{t_f^2(2\mu^s - \tau_0^s)}{2}(\tfrac{\partial^2 w}{\partial x^2}\tfrac{\partial^2\delta w}{\partial y^2} + \tfrac{\partial^2 w}{\partial y^2}\tfrac{\partial^2\delta w}{\partial x^2} - 2\tfrac{\partial^2 w}{\partial x\partial y}\tfrac{\partial^2\delta w}{\partial x\partial y})dxdy
\end{aligned}
\tag{B.1}
$$

Using the same method in Appendix A, one can rewrite Eq. (B.1) in the form:

$$
\begin{aligned}
\delta U_2 &= \iint \tfrac{(\lambda^s + 2\mu^s)t_f^2}{2}\nabla^4 w\delta w dxdy \\
&+ \int_S \tfrac{(\lambda^s + 2\mu^s)t_f^2}{2}[\tfrac{\partial^2 w}{\partial x^2}\cos^2\alpha + (\tfrac{\partial^2 w}{\partial y^2}\cos^2\alpha + \tfrac{\partial^2 w}{\partial x^2}\sin^2\alpha) + \tfrac{\partial^2 w}{\partial y^2}\sin^2\alpha] \\
&- \tfrac{t_f^2(2\mu^s - \tau_0^s)}{2}[(\tfrac{\partial^2 w}{\partial y^2}\cos^2\alpha + \tfrac{\partial^2 w}{\partial x^2}\sin^2\alpha) - 2\tfrac{\partial^2 w}{\partial x\partial y}\sin\alpha\cos\alpha]\tfrac{\partial\delta w}{\partial n}ds \\
&+ \int_S \tfrac{(\lambda^s + 2\mu^s)t_f^2}{2}
\left\{
\begin{array}{l}
[\tfrac{\partial}{\partial s}(\tfrac{\partial^2 w}{\partial x^2}\sin\alpha\cos\alpha) - \tfrac{\partial^3 w}{\partial x^3}\cos\alpha] \\
-\{\tfrac{\partial^3 w}{\partial x^2\partial y}\sin\alpha + \tfrac{\partial^3 w}{\partial x\partial y^2}\cos\alpha + \tfrac{\partial}{\partial s}[(\tfrac{\partial^2 w}{\partial x^2} - \tfrac{\partial^2 w}{\partial y^2}) \\
\sin\alpha\cos\alpha]\} - [\tfrac{\partial}{\partial s}(\tfrac{\partial^2 w}{\partial y^2}\sin\alpha\cos\alpha) + \tfrac{\partial^3 w}{\partial y^3}\sin\alpha]
\end{array}
\right\} \\
&+ \tfrac{t_f^2(2\mu^s - \tau_0^s)}{2}
\left\{
\begin{array}{l}
\{\tfrac{\partial^3 w}{\partial x^2\partial y}\sin\alpha + \tfrac{\partial^3 w}{\partial x\partial y^2}\cos\alpha + \tfrac{\partial}{\partial s}[(\tfrac{\partial^2 w}{\partial x^2} - \tfrac{\partial^2 w}{\partial y^2}) \\
\sin\alpha\cos\alpha]\} + \{\tfrac{\partial}{\partial s}[\tfrac{\partial^2 w}{\partial x\partial y}(\sin^2\alpha - \cos^2\alpha)] \\
-\tfrac{\partial^3 w}{\partial x\partial y^2}\cos\alpha - \tfrac{\partial^3 w}{\partial x^2\partial y}\sin\alpha\}
\end{array}
\right\}\delta wds
\end{aligned}
\tag{B.2}
$$

Then δU_2 reads

$$
\delta U_2 = \iint \frac{(\lambda^s + 2\mu^s)t_f^2}{2}\nabla^4 w\delta w dxdy + \int_S \Psi_1 \frac{\partial\delta w}{\partial n}ds + \int_S \Psi_2\delta wds
\tag{B.3}
$$

References

[1] D.H. Ho, Q. Sun, S.Y. Kim, J.T. Han, D.H. Kim, J.H. Cho, Stretchable and multimodal all graphene electronic skin, Adv. Mater. 28 (2016) 2601.

[2] C. Hou, H. Wang, Q. Zhang, Y. Li, M. Zhu, Highly conductive, flexible, and compressible all-graphene passive electronic skin for sensing human touch, Adv. Mater. 26 (2014) 5018–5024.

[3] Q.H. Wang, K. Kalantar-Zadeh, A. Kis, J.N. Coleman, M.S. Strano, Electronics and optoelectronics of two-dimensional transition metal dichalcogenides, Nat. Nanotechnol. 7 (2012) 699.

[4] J. Wang, L. Wu, X. Chen, W. Zhuo, G. Wang, Avoiding blister defects in low-stress hydrogenated amorphous silicon films for MEMS sensors, Sens. Actuators A Phys. 276 (2018) 11–16.

[5] L. Zhang, X. Zhang, J. Song, H. Zheng, Thermal fracture parameter analysis of MEMS multilayer structures based on the generalized thermoelastic theory, Microelectron. Reliab. 98 (2019) 106–111.

[6] R. Saha, Z. Xue, Y. Huang, W.D. Nix, Indentation of a soft metal film on a hard substrate: strain gradient hardening effects, J. Mech. Phys. Solids 49 (2001) 1997–2014.

[7] T. Niu, G. Cao, C. Xiong, Indentation behavior of the stiffest membrane mounted on a very compliant substrate: graphene on PDMS, Int. J. Solids Struct. 132-133 (2018) 1–8.

[8] Y. Liu, Y. Wei, H. Long, Identifying the viscoelastic properties of soft matter from the indentation response of a hard film-soft substrate system, Sci. China Phys. Mech. Astron. 63 (2020) 1–11.

[9] H. Xie, Y. Kang, H. Song, J. Guo, Q. Zhang, *In situ* method for stress measurements in film-substrate electrodes during electrochemical processes: key role of softening and stiffening, Acta Mech. Sin. 36 (2020) 1319–1335.

[10] B. Nie, S. Liu, Q. Qu, Y. Zhang, M. Zhao, J. Liu, Bio-inspired flexible electronics for smart E-skin, Acta Biomater. 139 (2022) 280–295.

[11] S. Park, M. Vosguerichian, Z. Bao, A review of fabrication and applications of carbon nanotube film-based flexible electronics, Nanoscale 5 (2013) 1727–1752.

[12] Z. Ma, Y. Zhou, S. Long, C. Lu, On the intrinsic hardness of a metallic film/substrate system: indentation size and substrate effects, Int. J. Plast. 34 (2012) 1–11.

[13] M. Li, H. Zhang, Z. Zhao, X. Feng, Surface effects on cylindrical indentation of a soft layer on a rigid substrate, Acta Mech. Sin. 36 (2020) 422–429.

[14] M.F. Doerner, W.D. Nix, A method for interpreting the data from depth-sensing indentation instruments, J. Mater. Res. 1 (2011) 601–609.

[15] H. Gao, C. Cheng-Hsin, L. Jin, Elastic contact versus indentation modeling of multi-layered materials, Int. J. Solids Struct. 29 (1992) 2471–2492.

[16] H. Xu, G.M. Pharr, An improved relation for the effective elastic compliance of a film/substrate system during indentation by a flat cylindrical punch, Scr. Mater. 55 (2006) 315–318.

[17] Y.F. Gao, H.T. Xu, W.C. Oliver, G.M. Pharr, Effective elastic modulus of film-on-substrate systems under normal and tangential contact, J. Mech. Phys. Solids 56 (2008) 402–416.

[18] Y. Liu, Y. Wei, P. Chen, Characterization of mechanical properties of two-dimensional materials mounted on soft substrate, Int. J. Mech. Sci. 151 (2019) 214–221.

[19] F. Box, C. Jacquemot, M. Adda-Bedia, D. Vella, Cloaking by coating: how effectively does a thin, stiff coating hide a soft substrate? Soft Matter 16 (2020) 4574–4583.

[20] H.P.A. Ali, A. Budiman, Advances in *In situ* microfracture experimentation techniques: a case of nanoscale metal–metal multilayered materials, J. Mater. Res. 34 (2019) 1449–1468.

[21] R. Taguchi, N. Akamatsu, K. Kuwahara, K. Tokumitsu, Y. Kobayashi, M. Kishino, K. Yaegashi, J. Takeya, A. Shishido, Nanoscale analysis of surface bending strain in film substrates for preventing fracture in flexible electronic devices, Adv. Mater. Interfaces 8 (2021) 2001662.

[22] V. Stoica, N. Laanait, C. Dai, Z. Hong, Y. Yuan, Z. Zhang, S. Lei, M. McCarter, A. Yadav, A. Damodaran, Optical creation of a supercrystal with three-dimensional nanoscale periodicity, Nat. Mater. 18 (2019) 377–383.

[23] X.L. Gao, G. Zhang, in: A Microstructure-And Surface Energy-Dependent Third-Order Shear Deformation Beam Model, 66, Zeitschrift für angewandte Mathematik und Physik, 2015, pp. 1871–1894.

[24] Y.G. Wei, J.W. Hutchinson, Hardness trends in micron scale indentation, J. Mech. Phys. Solids 51 (2003) 2037–2056.

[25] D.C. Lam, F. Yang, A. Chong, J. Wang, P. Tong, Experiments and theory in strain gradient elasticity, J. Mech. Phys. Solids 51 (2003) 1477–1508.

[26] G.Z. Voyiadjis, Y. Song, Strain gradient continuum plasticity theories: theoretical, numerical and experimental investigations, Int. J. Plast. 121 (2019) 21–75.

[27] R. Barretta, F.M. De Sciarra, Constitutive boundary conditions for nonlocal strain gradient elastic nano-beams, Int. J. Eng. Sci. 130 (2018) 187–198.

[28] L. Lu, X. Guo, J. Zhao, A unified size-dependent plate model based on nonlocal strain gradient theory including surface effects, Appl. Math. Model. 68 (2019) 583–602.

[29] Y. Liu, H. Ma, H. Long, Y. Wei, Couple effect of surface energy and strain gradient on the mechanical behaviors of the biological staggered composites, Compos. Struct. 271 (2021) 114133.

[30] F. Zhang, R. Saha, Y. Huang, W. Nix, K. Hwang, S. Qu, M. Li, Indentation of a hard film on a soft substrate: strain gradient hardening effects, Int. J. Plast. 23 (2007) 25–43.

[31] S. Chen, L. Liu, T. Wang, Small scale, grain size and substrate effects in nano-indentation experiment of film–substrate systems, Int. J. Solids Struct. 44 (2007) 4492–4504.

[32] Y. Liu, H. Ma, Y. Wei, P. Chen, Size effect investigation of indentation response of stiff film/compliant substrate composite structure, Int. J. Solids Struct. 193 (2020) 106–116.

[33] I. Vardoulakis, G. Exadaktylos, E. Aifantis, Gradient elasticity with surface energy: mode-III crack problem, Int. J. Solids Struct. 33 (1996) 4531–4559.

[34] M. Salamat-talab, F. Shahabi, A. Assadi, Size dependent analysis of functionally graded microbeams using strain gradient elasticity incorporated with surface energy, Appl. Math. Model. 37 (2013) 507–526.

[35] M. Shaat, A. Abdelkefi, Size dependent and micromechanical modeling of strain gradient-based nanoparticle composite plates with surface elasticity, Eur. J. Mech. A Solids 58 (2016) 54–68.

[36] S.K. Jena, S. Chakraverty, M. Malikan, F. Tornabene, Stability analysis of single-walled carbon nanotubes embedded in winkler foundation placed in a thermal environment considering the surface effect using a new refined beam theory, Mech. Based Des. Struct. Mach. 49 (2021) 581–595.

[37] K.T. Ho, S.F. Leung, T.Y. Li, P. Maity, B. Cheng, H.C. Fu, O.F. Mohammed, J.H. He, Surface effect on 2D hybrid perovskite crystals: perovskites using an ethanolamine organic layer as an example, Adv. Mater. 30 (2018) 1804372.

[38] Y. Shi, Modeling of nonlinear magnetoelectric coupling in layered magnetoelectric nanocomposites with surface effect, Compos. Struct. 185 (2018) 474–482.

[39] Y. Yan, S. Zhang, Y. Liu, Indentation behavior of a hard film resting on a soft substrate, Mech. Solids 56 (2021) 1140–1151.

[40] H. Georgiadis, I. Vardoulakis, E. Velgaki, Dispersive Rayleigh-wave propagation in microstructured solids characterized by dipolar gradient elasticity, J. Elast. 74 (2004) 17–45.

[41] X. Gao, H. Ma, Solution of Eshelby's inclusion problem with a bounded domain and Eshelby's tensor for a spherical inclusion in a finite spherical matrix based on a simplified strain gradient elasticity theory, J. Mech. Phys. Solids 58 (2010) 779–797.

[42] R.D. Mindlin, Micro-structure in linear elasticity, Arch. Ration. Mech. Anal. 16 (1964) 51–78.

[43] T.Q. Lu, W.X. Zhang, T. Wang, The surface effect on the strain energy release rate of buckling delamination in thin film–substrate systems, Int. J. Eng. Sci. 49 (2011) 967–975.

[44] M.E. Gurtin, A.I. Murdoch, A continuum theory of elastic material surfaces, Arch. Ration. Mech. Anal. 57 (1975) 291–323.

[45] J. Wang, Z. Huang, H. Duan, S. Yu, X. Feng, G. Wang, W. Zhang, T. Wang, Surface stress effect in mechanics of nanostructured materials, Acta Mech. Solida Sin. 24 (2011) 52–82.
[46] J. He, C.M. Lilley, Surface effect on the elastic behavior of static bending nanowires, Nano Lett. 8 (2008) 1798–1802.
[47] D. Ziane, M.H. Cherif, C. Cattani, K. Belghaba, Yang-Laplace decomposition method for nonlinear system of local fractional partial differential equations, Appl. Math. Nonlinear Sci. 4 (2019) 489–502.
[48] H. Chen, X. Liu, G. Hu, Overall plasticity of micropolar composites with interface effect, Mech. Mater. 40 (2008) 721–728.
[49] G. Jing, H.L. Duan, X. Sun, Z. Zhang, J. Xu, Y. Li, J. Wang, D. Yu, Surface effects on elastic properties of silver nanowires: contact atomic-force microscopy, Phys. Rev. B 73 (2006) 235409.
[50] S. Cuenot, C. Frétigny, S. Demoustier-Champagne, B. Nysten, Surface tension effect on the mechanical properties of nanomaterials measured by atomic force microscopy, Phys. Rev. B 69 (2004) 165410.
[51] C. Chen, Y. Shi, Y.S. Zhang, J. Zhu, Y. Yan, Size dependence of Young's modulus in ZnO nanowires, Phys. Rev. Lett. 96 (2006) 075505.
[52] Z. Tan, J. Guo, The unified solution of infinite plate on elastic foundation, Chin. J. Appl. Mech. 33 (2016) 9.
[53] X.L. Gao, S.S. Zhou, in: Strain Gradient Solutions of Half-Space and Half-Plane Contact Problems, 64, Ztschrift für angewandte Mathematik und Physik, 2013, pp. 1363–1386.
[54] J. Song, J. Liu, H. Ma, L. Liang, Y. Wei, Determinations of both length scale and surface elastic parameters for fcc metals, C.R. Mec. 342 (2014) 315–325.
[55] V.B. Shenoy, Atomistic calculations of elastic properties of metallic fcc crystal surfaces, Phys. Rev. B 71 (2005) 094104.
[56] G. Cao, Y. Liu, T. Niu, Indentation response of two-dimensional materials mounted on different substrates, Int. J. Mech. Sci. 137 (2018) 96–104.
[57] S. Suresh, T.G. Nieh, B. Choi, Nano-indentation of copper thin films on silicon substrates, Scr. Mater. 41 (1999) 951–957.
[58] D.Y. Yu, F. Spaepen, The yield strength of thin copper films on Kapton, J. Appl. Phys. 95 (2004) 2991–2997.
[59] X. Wei, D. Lee, S. Shim, X. Chen, J.W. Kysar, Plane-strain bulge test for nanocrystalline copper thin films, Scr. Mater. 57 (2007) 541–544.
[60] J. Song, Y. Wei, A method to determine material length scale parameters in elastic strain gradient theory, J. Appl. Mech. 87 (2020) 031010.